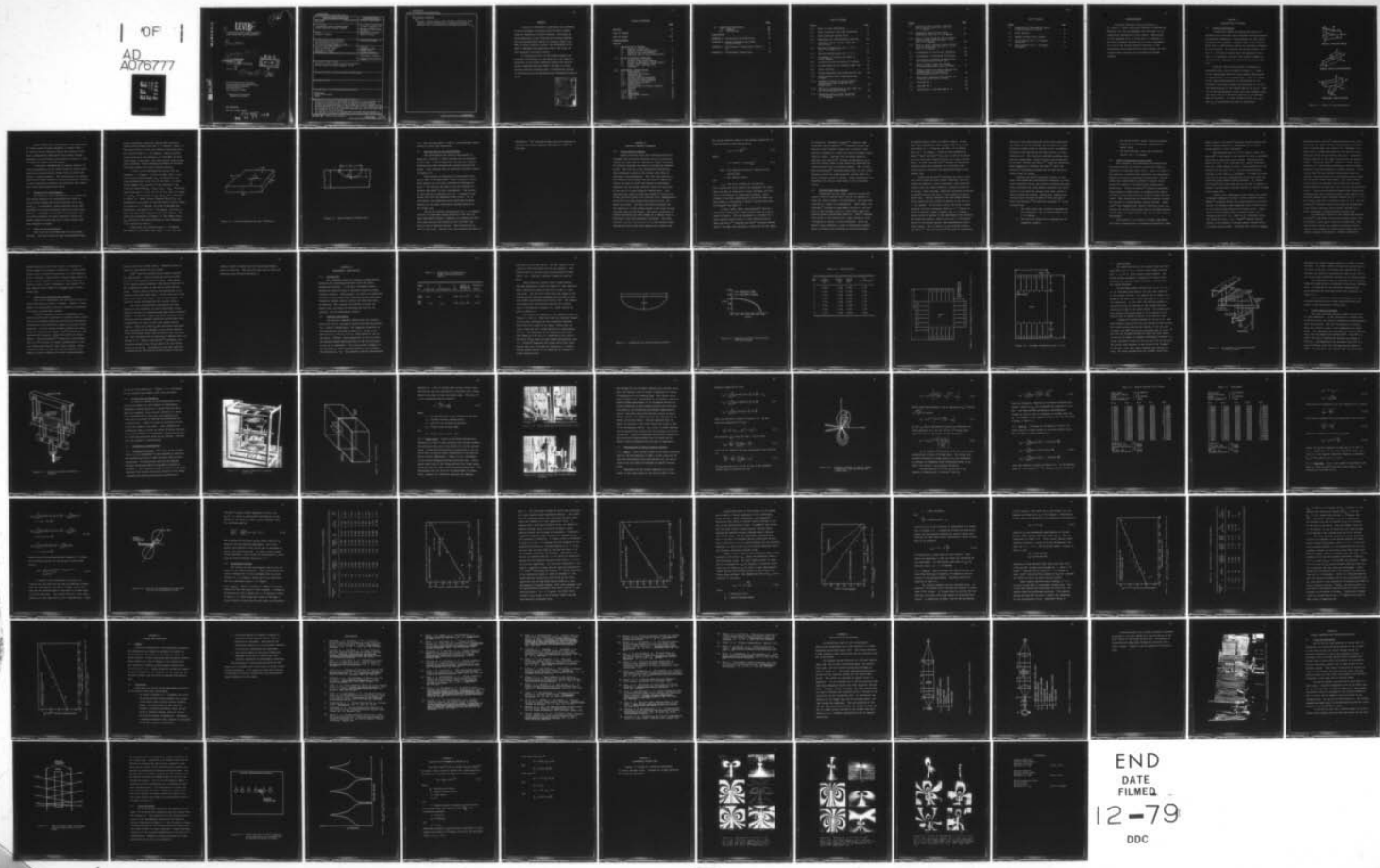


AD-A076 777 PENNSYLVANIA STATE UNIV UNIVERSITY PARK APPLIED RESE--ETC F/8 13/8
A PHOTOLELASTIC STUDY OF SURFACE-FLAWED PLATES SUBJECTED TO BIAX--ETC(U)
SEP 78 M L BASEMORE N00017-73-C-1418

UNCLASSIFIED TM-78-228 NL

| OF |
AD
A076777



END
DATE
FILED
12-79
DDC

ADA 076777

LEVELY

A PHOTOELASTIC STUDY OF SURFACE-FLAWED
PLATES SUBJECTED TO BIAXIAL LOADINGS

Michael L. Basehore

⑨ Master's thesis,

Technical Memorandum

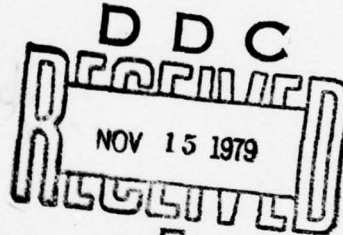
File No. TM-78-228

September 5, 1978

Contract No. N00017-73-C-1418

Copy No.

5



⑩ 5 sep 78 (B) 93

The Pennsylvania State University
Institute for Science and Engineering
APPLIED RESEARCH LABORATORY
Post Office Box 30
State College, PA 16801

APPROVED FOR PUBLIC RELEASE
DISTRIBUTION UNLIMITED

DDC FILE COPY

NAVY DEPARTMENT

NAVAL SEA SYSTEMS COMMAND

391 007 002
79 11 15 yb

UNCLASSIFIED

SECURITY CLASSIFICATION OF THIS PAGE (When Data Entered)

REPORT DOCUMENTATION PAGE		READ INSTRUCTIONS BEFORE COMPLETING FORM
1. REPORT NUMBER TM 78-228	2. GOVT ACCESSION NO.	3. RECIPIENT'S CATALOG NUMBER
4. TITLE (and Subtitle) A PHOTOELASTIC STUDY OF SURFACE-FLAWED PLATES SUBJECTED TO BIAXIAL LOADINGS		5. TYPE OF REPORT & PERIOD COVERED MS Thesis, November 1978
7. AUTHOR(s) Michael L. Basehore		6. PERFORMING ORG. REPORT NUMBER TM 78-228
9. PERFORMING ORGANIZATION NAME AND ADDRESS The Pennsylvania State University Applied Research Laboratory P. O. Box 30, State College, PA 16801		10. PROGRAM ELEMENT, PROJECT, TASK AREA & WORK UNIT NUMBERS
11. CONTROLLING OFFICE NAME AND ADDRESS Naval Sea Systems Command Department of the Navy Washington, DC 20362		12. REPORT DATE September 5, 1978
14. MONITORING AGENCY NAME & ADDRESS (if different from Controlling Office)		13. NUMBER OF PAGES 91 pages & figures
		15. SECURITY CLASS. (of this report) Unclassified, Unlimited
		15a. DECLASSIFICATION/DOWNGRADING SCHEDULE
16. DISTRIBUTION STATEMENT (of this Report) Approved for public release, distribution unlimited, per NSSC (Naval Sea Systems Command), 9/27/78		
17. DISTRIBUTION STATEMENT (of the abstract entered in Block 20, if different from Report)		
18. SUPPLEMENTARY NOTES		
19. KEY WORDS (Continue on reverse side if necessary and identify by block number) photoelastic surface-flawed plates biaxial		
20. ABSTRACT (Continue on reverse side if necessary and identify by block number) A series of photoelastic experiments was performed on plate specimens containing semi-elliptical surface flaws and subjected to biaxial bending. Utilizing the three-dimensional stress freezing and slicing technique and the Schroedl-Smith ² method of analysis, Mode I and Mode II stress intensity factors were determined at the point of maximum flaw penetration and at the point the flaw intersects the plate surface. By varying the ratio of the bending moments perpendicular and parallel to the crack axis, the effect of biaxiality on the stress intensity factors was		

UNCLASSIFIED

SECURITY CLASSIFICATION OF THIS PAGE(When Data Entered)

20 ABSTRACT (CONTINUED)

observed. Results indicated that both Mode I and Mode II stress intensity factors increased with a corresponding increase in biaxiality ratio and decreased with decreasing biaxiality ratio.

UNCLASSIFIED

SECURITY CLASSIFICATION OF THIS PAGE(When Data Entered)

ABSTRACT

A series of photoelastic experiments was performed on plate specimens containing semi-elliptical surface flaws and subjected to biaxial bending. Utilizing the three-dimensional stress freezing and slicing technique and the Schroedl-Smith² method of analysis, Mode I and Mode II stress intensity factors were determined at the point of maximum flaw penetration and at the point the flaw intersects the plate surface.

By varying the ratio of the bending moments perpendicular and parallel to the crack axis, the effect of biaxiality on the stress intensity factors was observed. Results indicated that both Mode I and Mode II stress intensity factors increased with a corresponding increase in biaxiality ratio and decreased with decreasing biaxiality ratio.

Accession No.	
NTIS G-141	<input checked="" type="checkbox"/>
DDC TAB	<input checked="" type="checkbox"/>
Unannounced	<input type="checkbox"/>
Justification	
By _____	
Distribution	
Availability Codes	
Dist	Avail and/or special
A	

TABLE OF CONTENTS

	<u>Page</u>
ABSTRACT	iii
LIST OF FIGURES	vi
LIST OF TABLES	viii
ACKNOWLEDGMENTS	ix
 CHAPTER	
I. INTRODUCTION TO PROBLEM	1
1.1 General Introduction	1
1.2 Purpose of the Investigation	3
1.3 Scope of the Investigation	3
1.4 Approach Used in the Investigation	7
II. REVIEW OF RELATED LITERATURE	9
2.1 Surface Flaw in Tension	9
2.2 Surface Flaws Under Bending	11
2.3 Cracks in Multiaxial Stress Fields	14
2.4 Cracks Under Combined Mode Loadings	17
III. EXPERIMENTAL INVESTIGATION	20
3.1 Introduction	20
3.2 Materials and Models	20
3.3 Loading Frame	28
3.4 Stress Freezing Procedure	30
3.5 Slicing Plan and Technique	32
3.6 Photoelastic Investigation	32
3.6.1 Calibration Specimen	32
3.6.2 Model Slices	35
3.7 Determination of Stress Intensity Factors	37
3.7.1 Mode I	37
3.7.2 Mode II	41
3.7.3 Mixed-Mode	44
3.8 Experimental Results	47
3.8.1 Case I	47
3.8.2 Case II	54

	<u>Page</u>
IV. SUMMARY AND CONCLUSIONS	60
4.1 Summary	60
4.2 Conclusions	60
BIBLIOGRAPHY	62
APPENDIX A - Construction of Polariscopic	67
APPENDIX B - Fringe Sharpening and Fringe Multiplication	72
APPENDIX C - Calculation of Theoretical Values of K_I	77
APPENDIX D - Isochromatic Fringe Loops	79

LIST OF FIGURES

<u>Figure</u>		<u>Page</u>
1.1	Modes of crack deformation	2
1.2	Crack orientation and sign convention . .	5
1.3	Semi-elliptical surface flaw	6
3.1	Dimensions for semi-elliptical profile . .	23
3.2	Comparison beteen natural crack and semi-ellipse	24
3.3	Specimen configuration for $\Phi = +1.0,$ $+0.5, -0.5,$ and -1.0	26
3.4	Specimen configuration for $\Phi = 0.0$. . .	27
3.5	Arrangement of loading the model by nylon filament	29
3.6	Calibration beam and method of loading . .	31
3.7	Loading frame with a specimen under load .	33
3.8	Slice locations	34
3.9	Fringe sharpening and multiplication unit.	36
3.10	Telemicroscope with fringe measuring eyepiece	36
3.11	Schematic drawing of typical fringe pattern with sign convention and nomenclature	39
3.12	Sketch of isochromatics at the crack tip for the mixed-mode problem	46
3.13	Normalized Mode I stress intensity factor versus biaxiality ratio for $\alpha = 90$ degrees	49

<u>Figure</u>	<u>Page</u>
3.14 Normalized Mode I stress intensity factor versus biaxiality ratio for $\alpha = 0$ degrees	51
3.15 Normalized remote stress versus biaxiality ratio for $\alpha = 90$ degrees	53
3.16 Mode I stress intensity factor versus distance from crack tip for $\phi = 0.0$ and $\alpha = 90$ degrees	56
3.17 Mode II stress intensity factor versus distance from crack tip for $\phi = -1.0$ and $\alpha = 90$ degrees	59
A.1 Arrangement of polariscope components	68
A.2 Arrangement of renovated polariscope	69
A.3 Polariscope, including telemicroscope and fringe multiplication unit	71
B.1 Path of single light ray through fringe multiplication unit and model	73
B.2 Proper location of source aperture for optimum angle of incidence for a multiplication factor of seven	75
B.3 Dark field intensity distribution for sharpened isochromatic fringes	76
D.1 Specimen No. 1	80
D.2 Specimen No. 5	81
D.3 Specimen No. 4 and Specimen No. 8	82

LIST OF TABLES

<u>Table</u>		<u>Page</u>
3.1	Properties of Photoelastic Stress Freezing Material, PLM-1Z	21
3.2	Model Details	25
3.3	Sample Printout of K_I Values	42
3.4	Slice Details for $\theta = 0$ Degree Specimens	48
3.5	Slice Details for $\theta = 45$ Degree Specimens	57

ACKNOWLEDGMENTS

The author expresses sincere gratitude to Dr. Joseph C. Conway, Associate Professor of Engineering Mechanics, for his encouragement and assistance in the research and preparation of this thesis. Appreciation is also extended to R. J. Olson and N. D. Ghadiali of Battelle's Columbus Laboratories for their programming aid, and to the Applied Research Laboratory of The Pennsylvania State University for their support for this research under contract with the Naval Sea Systems Command.

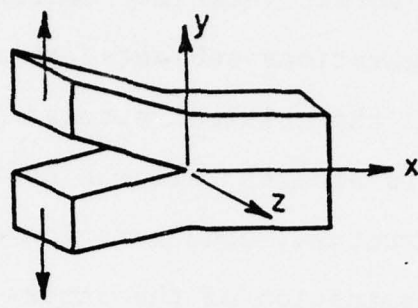
CHAPTER I

INTRODUCTION TO PROBLEM

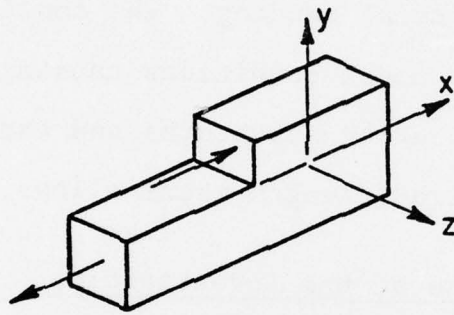
1.1 General Introduction

A significant amount of engineering research is currently being directed toward problems involving fracture of structural components. These failures are very often associated with induced or inherent flaws in the material which tend to significantly reduce the calculated strength of the structure. By utilizing the stress intensity factor, K , a function of applied load and geometry of the flaw, it is possible to predict the reduced strength of the structural components and therefore the entire structure.

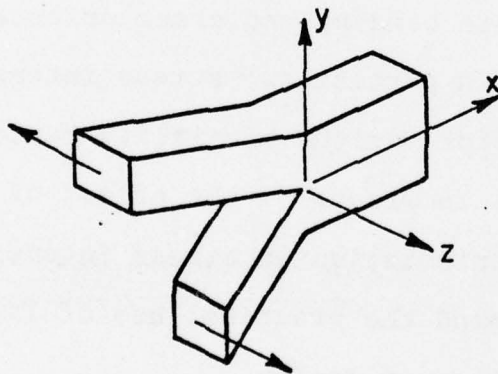
There are three possible modes of deformation associated with a crack as shown in Figure 1.1. Mode I is the opening mode where the crack surface displacement is perpendicular to the loading plane. Mode II is known as the edge sliding mode and is characterized by the surfaces of the crack sliding over each other in a direction perpendicular to the leading edge of the crack. Mode III is the tearing mode in which the crack surfaces slide over each other in a direction parallel to the leading edge of the crack. A stress intensity factor, K_I , K_{II} , and K_{III} is associated with each of these modes.



MODE I, OPENING MODE



MODE II, EDGE SLIDING MODE



MODE III, TEARING MODE

Figure 1.1. Modes of crack deformation.

Recent efforts have concentrated on the application of linear elastic fracture mechanics to predict Mode I, II, and III stress intensity factors for realistic structural configurations subjected to anticipated loadings. Knowledge of the critical stress intensity factor, K_c , for the materials assures reliable design.

A structural configuration of current interest involves determination of the stress intensity factors associated with semi-elliptical surface flaws in plates subjected to uniaxial bending. The configuration and loading realistically model conditions causing catastrophic failures in many engineering structures and especially those fabricated from high-strength metal alloys.

1.2 Purpose of the Investigation

The purpose of this investigation is to extend current design capability by establishing the effect of biaxial plate bending and crack orientation on K_I , K_{II} , and K_{III} . In particular, stress intensity factors were determined for various biaxiality ratios and crack orientations. A knowledge of the effect of biaxiality ratio and crack orientation on stress intensity factors will greatly expand the practical use of linear elastic fracture mechanics in design.

1.3 Scope of the Investigation

This study will be broken down into two primary sections. The first series of tests was performed using

plates containing a centrally located semi-elliptical surface crack oriented such that $\theta = 0$ degrees, Figure 1.2. The second series of tests was conducted utilizing plates with similar flaws at $\theta = 45$ degrees. Special consideration was given to the selection of a procedure by which crack length, crack depth, and crack profile could be kept nearly constant, thereby reducing the number of variables which might affect the stress intensity factors.

A total of five specimens were tested with the parameter $\theta = 0$ degrees. In each of these tests, a positive constant bending moment, M_{xx} , was applied to the plate perpendicular to the line of the crack. A second bending moment, M_{yy} , parallel to the direction of the crack was varied from $M_{yy} = +M_{xx}$ to $M_{yy} = -M_{xx}$. The actual test values were $\phi = +1.0, +0.5, 0.0, -0.5$, and -1.0 , where $\phi = M_{yy}/M_{xx}$ and directions of M_{xx} and M_{yy} are illustrated in Figure 1.2. Mode I stress intensity factor, K_I , was determined at two points on the crack front; Point A, which is located at $\alpha = 0$ degrees, the point of maximum flaw penetration, and Point B at $\alpha = 90$ degrees, the point at which the crack front intersects the plate surface. Both points are illustrated in Figure 1.3. The remote stress, σ_{ox} , parallel to the crack direction was also determined in the vicinity of Point B.

Three tests were conducted with $\theta = 45$ degrees. The values of ϕ for these tests were $\phi = +1.0, 0.0$, and

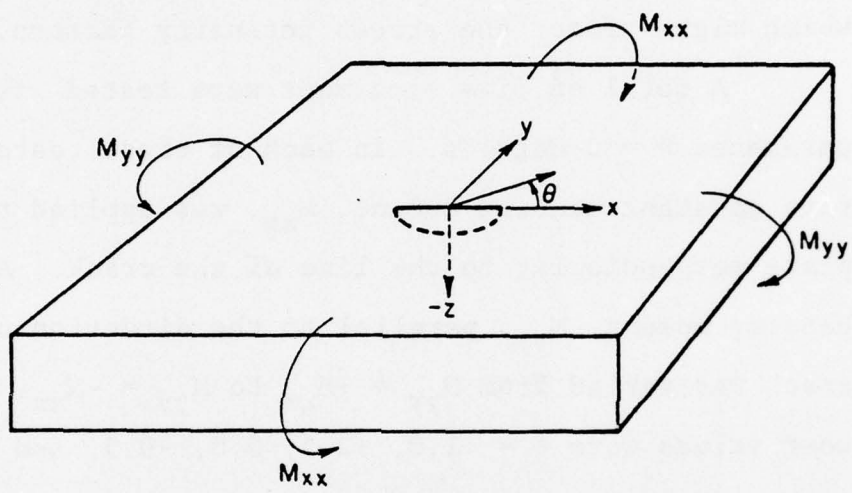


Figure 1.2. Crack orientation and sign convention.

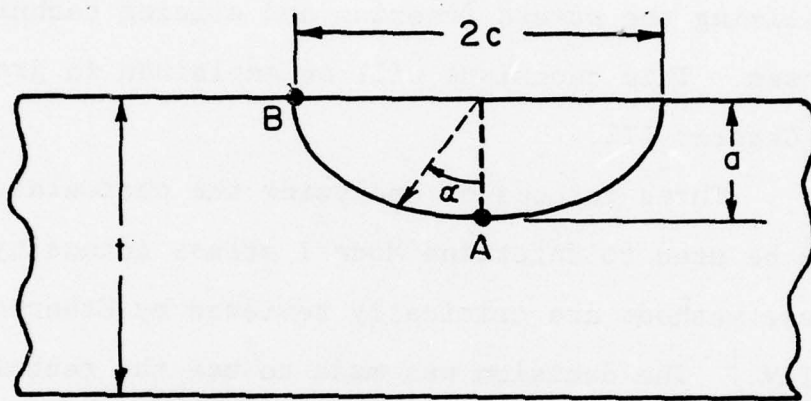


Figure 1.3. Semi-elliptical surface flaw.

-1.0. The resulting Mode I, Mode II, and mixed-mode stress intensity factors were determined.

1.4 Approach Used in the Investigation

The investigation was entirely experimental as analytical solutions to these problems are not available at this time. A three-dimensional photoelastic analysis utilizing the stress freezing and slicing technique was chosen. This technique will be explained in greater detail in Chapter III.

Three methods of analyzing the photoelastic data can be used to determine Mode I stress intensity factors.

These methods are critically reviewed by Etheridge and Dally.¹ The decision was made to use the technique of Schroedl and Smith² in this investigation. The accuracy of this method is predicted to be $K_I \pm 5$ percent if the fringe loop radii are measured without error. Use of this method also eliminates errors involving the determination of the angle locating the extreme position of the fringe loop.

One of the loading configurations for $\theta = 45$ degrees resulted in mixed-mode fringe patterns at the crack tip.

Smith and Smith³ devised a technique for reducing the data from these patterns and obtaining both the Mode I and Mode II stress intensity factors. Their method will be used in this paper. Another load case produced pure Mode II

deformation. The resulting fringe loops were analyzed by utilizing the stress equations developed by Irwin⁴ for this mode.

CHAPTER II

REVIEW OF RELATED LITERATURE

2.1 Surface Flaw in Tension

During the first forty years following Griffith's findings⁵ that the actual fracture stress of brittle materials was lower than the theoretical values calculated, all fracture analyses were based on through-the-thickness cracks. This was due to the difficulties encountered when attempting to analyze the surface crack which is inherently three-dimensional. The first contribution to the problem of the surface flaw subjected to remote extension was made by Irwin⁶ who derived an approximate expression for the stress intensity factor for any point on the edge of a semi-elliptical surface crack. This derivation was based on Green and Sneddon's⁷ solution for a flat elliptical crack in an infinite solid, Wigglesworth's solution⁸ of an edge-cracked semi-infinite solid, and three corrections. The first correction accounted for the addition of a free surface normal to the crack through the major axis of the ellipse. The second correction considered increasing the crack length by an amount equal to the plastic zone size previously calculated. The final correction was for the presence of the free surface representing the side of the plate opposite the surface flaw.

The stress intensity factor at the deepest penetration of a semi-elliptical crack was given by:

$$K_I = 1.1\sigma \left(\frac{\pi a}{Q}\right)^{1/2}, \quad (2.1)$$

where

$$Q = [E(k)]^2 - 0.212\left(\frac{\sigma}{\sigma_{ys}}\right)^2, \quad (2.2)$$

$E(k)$ = the complete elliptical integral of the second kind,

σ = the applied stress ,

and

σ_{ys} = the yield strength of the material.

This solution was later found to be inadequate for flaws which are deep in comparison to plate thickness and fracture in the presence of large-scale yielding. Early attempts to estimate magnification factors for deep surface flaws as a correction to Irwin's solution were made by Kobayashi⁹ and Smith.¹⁰

In 1967, Smith, Emery, and Kobayashi¹¹ derived a theoretical solution for a semi-circular flaw in a half-space in tension. This was extended to a solution for a part-circular surface flaw in a semi-infinite solid by Smith and Alavi.¹² Kobayashi and Moss¹³ presented further work in the same area including a correction for the effect

of plasticity. Thresher and Smith,¹⁴ using the same techniques applied earlier,^{11,12} extended the work and derived stress intensity factors for a circular crack partially embedded in a solid with finite thickness under tensile loading. Separate from the above method of approach, Rice and Levy¹⁵ obtained an approximate solution for surface flaws in pure tension by replacing the cracked section with a continuous spring. Then in 1973, Shah and Kobayashi¹⁶ developed expressions for the stress intensity factor for semi-elliptical surface flaws in a finite thickness plate in tension. These expressions were determined for various crack depth to plate thickness ratios.

2.2 Surface Flaws Under Bending

Expressions for the stress intensity factors for surface flaws in bending fields are not as numerous as those for tensile fields, but nonetheless, they have been obtained by a number of investigators. Smith, Emery, and Kobayashi¹¹ provided an approximate solution to the problem of semi-circular crack in a half-space under pure bending using an alternating technique. Smith¹⁰ extended this result to the solution for a semi-elliptical crack in bending in a plate of finite thickness. Marrs and Smith¹⁷ later conducted a series of photoelastic experiments utilizing stress freezing and slicing techniques

and compared their results to Smith's theory. It was found that experimental values ranged from 12 to 24 percent higher at $\alpha = 0$ degrees and from 7 to 19 percent lower at $\alpha = 90$ degrees. Using the same technique as Smith,¹¹ Smith and Alavi¹² were able to derive an expression for the stress intensity factor for a part-circular crack. In 1970, Rice and Levy¹⁵ obtained an approximate solution using their technique of a continuous line-spring model to represent the bending resistance of the surface flaw.

Grandt and Sinclair¹⁸ determined the stress intensity factor where the crack border intersects the plate surface by modeling a plate containing a semi-elliptical surface crack as a beam containing a spring in place of the crack. Their findings, along with analytical solutions by Smith¹⁰ and Rice and Levy,¹⁵ were compared to experimental data. Results indicated that the Grandt-Sinclair theory generally falls within 15 percent of the data for $\alpha = 90$ degrees. The Rice-Levy theory was found to underestimate the stress intensity factor at $\alpha = 0$ degrees by about 15 percent. Smith's analysis for $\alpha = 0$ degrees agreed within 10 percent of the experimental data obtained by Grandt and Sinclair, while results for $\alpha = 90$ degrees were 10 to 30 percent greater than experimentally determined values. This is similar to the findings of Marrs and Smith.¹⁷ Shah and Kobayashi¹⁹ obtained an approximate

solution to the semi-elliptical surface flaw problem for all values of a/t by utilizing the solutions for a semi-elliptical surface crack in tension and for an embedded elliptical flaw approaching the free surface of a semi-infinite solid. This solution exhibited excellent agreement with experimental results obtained photoelastically by Schroedl, McGowan, and Smith.²⁰ Using the alternating method suggested by Thresher and Smith,¹⁴ Smith and Sorenson²¹ determined an expression for semi-elliptical surface flaws in bending.

Schroedl and Smith² performed a series of tests using three-dimensional photoelastic techniques to obtain stress intensity factors near points of maximum flaw penetration and where the crack border intersects the tensile surface of the plate for natural flaws under fields of remote cylindrical bending. Results were compared with the analytical solutions of Smith,¹⁰ Rice and Levy,¹⁵ Grandt and Sinclair,¹⁸ and Shah and Kobayashi.¹⁹ It was concluded that:

1. The Smith theory was in general agreement for most geometries, but did underestimate K_I for $\alpha = 0$ degrees.
2. The Rice-Levy theory was not appropriate for geometries studied.

3. The Grandt-Sinclair theory yielded reasonable results at $\alpha = 90$ degrees, especially for deeper flaws.
4. The Shah-Kobayashi theory gave excellent results for $\alpha = 0$ degrees.

2.3 Cracks in Multiaxial Stress Fields

Until recently, most published work dealing with the stress analysis of cracks has dealt with flaws encountered in a uniaxial stress field. This is a result of the complexity associated with analytical and experimental analyses of cracks in multiaxial stress fields. Several authors have approached the problem of biaxial stress fields with regard to the effects upon fatigue-crack growth rates. Kibler and Roberts²² conducted experiments using biaxially loaded plates of aluminum alloys 6061-T6 and 6061-T4 containing centrally located through-thickness cracks. They demonstrated an increasing residual strength with increasing lateral biaxial tensile stresses. Adams' study²³ also suggested that tensile transverse stress can decrease the cyclic crack growth rate for through-thickness cracks, based on either plastic zone size or crack opening displacement.

More recently, in a series of fatigue experiments with center-cracked plates of polymethylmethacrylate (PMMA),

Radon, Leever, and Culver²⁴ obtained results showing that crack extension behavior is independent of the stress acting parallel to the crack plane.

The remaining point of view is taken by Joshi and Shewchuk²⁵ on the basis of the results of tests on aluminum alloy plates containing surface flaws. With biaxiality ratios of $\sigma_2/\sigma_1 = 1.0, 0.86$, and 0.75 , results indicated that for a given number of cycles, crack extension was the greatest for the case of $\sigma_2 = \sigma_1$ and decreased proportionally as the ratio σ_2/σ_1 decreased. It should be noted that this is the only investigation listed here which was conducted using surface cracked specimens. Oh, Vardar, and Finnie²⁶ have also shown that an increase in degree of biaxial tension-tension stresses results in a faster fatigue crack growth rate.

Several other investigators have studied the effect of biaxial loading on the Mode I stress intensity factor. Newman²⁷ presented results for stress-intensity correction factors for through cracks emanating from a circular hole in an infinite plate subjected to biaxial stress. These results showed highest stress intensity factors for a biaxiality ratio of -1.0, lower for 0.0 biaxiality ratio, and lowest for $\sigma_2/\sigma_1 = 1.0$. Grandt²⁸ obtained similar results in his studies of through-cracked fastener holes in biaxial stress fields. Utilizing the concept of strain

intensity factor, Hilton²⁹ presented results which indicated that for applied normal tractions beyond the small scale yielding range, the addition of a component of biaxial tensile loading decreases both the plastic strain intensity factor and the plastic zone size. Compressive loading parallel to the crack direction had the opposite effect. Miller and Kfouri³⁰ conducted a finite element analysis of a square plate containing a central through-thickness crack and subjected to biaxial stresses. Their results show the equi-biaxial loading mode causes the greatest separation stress but the smallest plastic shear ear and crack opening displacement. The shear loading system induces the maximum size of shear ear and crack displacement but the smallest value of crack tip separation stress. Using the relationship between crack opening displacement and stress intensity factor, these results would indicate highest stress intensity factors for $\sigma_2/\sigma_1 = -1.0$ and lowest values for a biaxiality ratio of +1.0. Lee and Liebowitz³¹ obtained results indicating the same general trend using a nonlinear finite element analysis for a plate containing a through-thickness center crack.

An analytical solution to the problem was obtained by Smith³² using plane stress-strain energy release rate. His results, which oppose those stated previously, show that biaxial tension, as compared to uniaxial tension, results in an increase in strain energy release with increase in degree of biaxiality. Biaxial compression

applied parallel to the crack results in a decrease in strain energy with increase in biaxiality. Strain energy release rate is directly proportional to stress intensity factor; therefore, these results indicate higher values of K_I for positive biaxiality ratios and lower values for negative ratios. Eftis, Subramonian, and Liebowitz³³ reveal similar results based on the local elastic strain energy rate.

2.4 Cracks Under Combined Mode Loadings

Most of the experimental and theoretical studies of cracks have dealt with Mode I loadings. However, a small number of investigations have been conducted to determine the effects of mixed-mode loadings.

Wilson³⁴ conducted a series of experiments with center-cracked plates subjected to a uniform tensile field. The ratio of combined modes was controlled by the angular orientation of the crack with respect to the stress field direction. Critical stress intensity factors were calculated for various crack angles. Pook³⁵ utilized the same specimen and loading on plates with cracks at various angles. Iida and Kobayashi³⁶ studied the crack propagation in 7075-T6 plates of similar configurations to the two studies mentioned but under cyclic loading. Stress intensity factors, K_I and K_{II} , were determined by the method of direct stiffness for curved cracks generated

from the initially slanted cracks. Propagation rates increased in the presence of K_{II} loading.

Shah³⁷ used the inclined center-cracked specimens for combined Mode I - Mode II loading and inclined surface flaws for combined Mode I-II-III loading. From results of the center-cracked specimens, Shah noticed that Mode II has a significant effect on the load at which fracture occurs. Stress intensity factors were determined at the surface of the plate where Modes I and II exist and at the base of the crack where Modes I and III are present. Interaction curves were generated for critical values.

Two sets of photoelastic experiments have been reported in the literature in which isochromatic fringe data have been used to determine mixed-mode stress intensity factors. In the first, Smith and Smith³ conducted stress freezing tests on specimens exhibiting various edge crack configurations in finite strips under remote tensile loading. Values of K_I and K_{II} were calculated using equations developed for the maximum in-plane local shearing stress and average fringe loop inclination near the crack tip. This procedure will be explained in greater detail in Section 3.7.3. Gdoutos and Theocaris³⁸ developed a new evaluation method of the fringe pattern for the determination of K_I and K_{II} . Extrapolation laws were given for transferring the far-from-the-crack-tip data to the near

region in order to bypass the error-prone measurements near the crack tip. This data was then used to solve the equations noted by Smith and Smith.³

CHAPTER III

EXPERIMENTAL INVESTIGATION

3.1 Introduction

The literature review has revealed an experimental procedure for obtaining photoelastic data for three-dimensional problems. It has also illustrated several methods of using this data to calculate crack-tip stress intensity factors. Unfortunately, the lack of an analytical solution to the problem under investigation does not allow comparison between results achieved and those that might be expected. This chapter will examine in detail the models used, the method of obtaining the data for the analysis, and the experimental results.

3.2 Materials and Models

The material originally selected for this investigation was PLM-1Z, obtained in liquid form from Photolastic, Inc., Malvern, Pennsylvania. Its suggested properties by the manufacturer are given in Table 3.1. It was to be cast in 12 in. x 12 in. x 3/4 in. thick plates by the investigator. However, after preparation of only one plate, the material became unavailable due to the discontinuance of one of its components. This necessitated a change to a new photoelastic stress freezing material, also obtained from Photolastic, Inc. This material requires substantially

Table 3.1. Properties of Photoelastic
Stress Freezing Material,
PLM-1Z

Temp. °F	E x 1000 psi	f_σ psi/fringe/in.	σ_y psi	Coeff. of expansion in./in./°F	Poisson's Ratio
room temp.	400	80	7500	39×10^{-6}	0.36
160- 180	1.8	1.8	>150	90×10^{-6}	0.50

more time to cast than PLM-1Z. For this reason, it was decided to have the plates cast by the supplier. This material has not yet been fully characterized by Photolastic, Inc.; therefore, material properties were not given.

Semi-elliptical surface flaws of approximately the same dimensions as shown in Figure 3.1 were simulated while casting the plates by the use of 0.005 in. thick shim stock. The end of the shim stock was shaped to the desired profile and then suspended over the mold so that this shaped end produced an artificial flaw. The comparison between this crack profile and that of a natural crack is illustrated in Figure 3.2. Model details are given in Table 3.2.

The plates were machined to the dimensions shown in Figures 3.3 and 3.4. Each plate had six extended "fingers" on each side, excluding the zero biaxiality specimens which were only loaded on two sides. Plates were cut using a band saw with a blade thickness of approximately 0.05 in. The dimensions of the remaining uncut plate were chosen as 6 in. by 6 in. resulting in the ratio of the width of the plate to crack length being greater than 3.0. Fichter³⁹ suggested that plates which have ratios greater than this value and are subjected to a uniform bending moment applied at its edges may be treated as a loaded infinite plate.

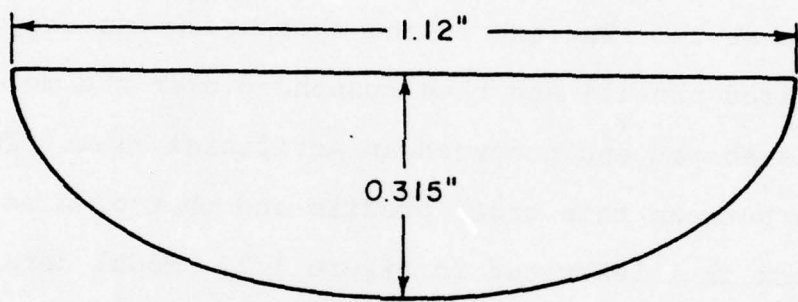


Figure 3.1. Dimensions for semi-elliptical profile.

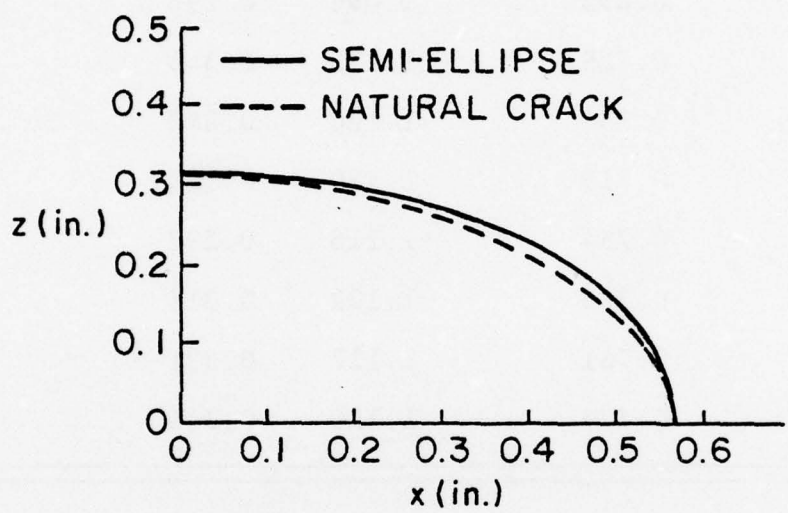


Figure 3.2. Comparison between natural crack and semi-ellipse.

Table 3.2. Model Details

Exp. No.	Plate Thickness in.	Crack Length in.	Crack Depth in.	f_{σ} psi/fringe/in.
1	0.695	1.090	0.296	1.20
2	0.728	1.115	0.346	2.36
3	0.734	1.120	0.340	2.30
4	0.719	1.120	0.328	2.45
5	0.754	1.118	0.292	2.34
6	0.726	1.122	0.319	2.50
7	0.761	1.117	0.331	3.26
8	0.779	1.120	0.346	2.60

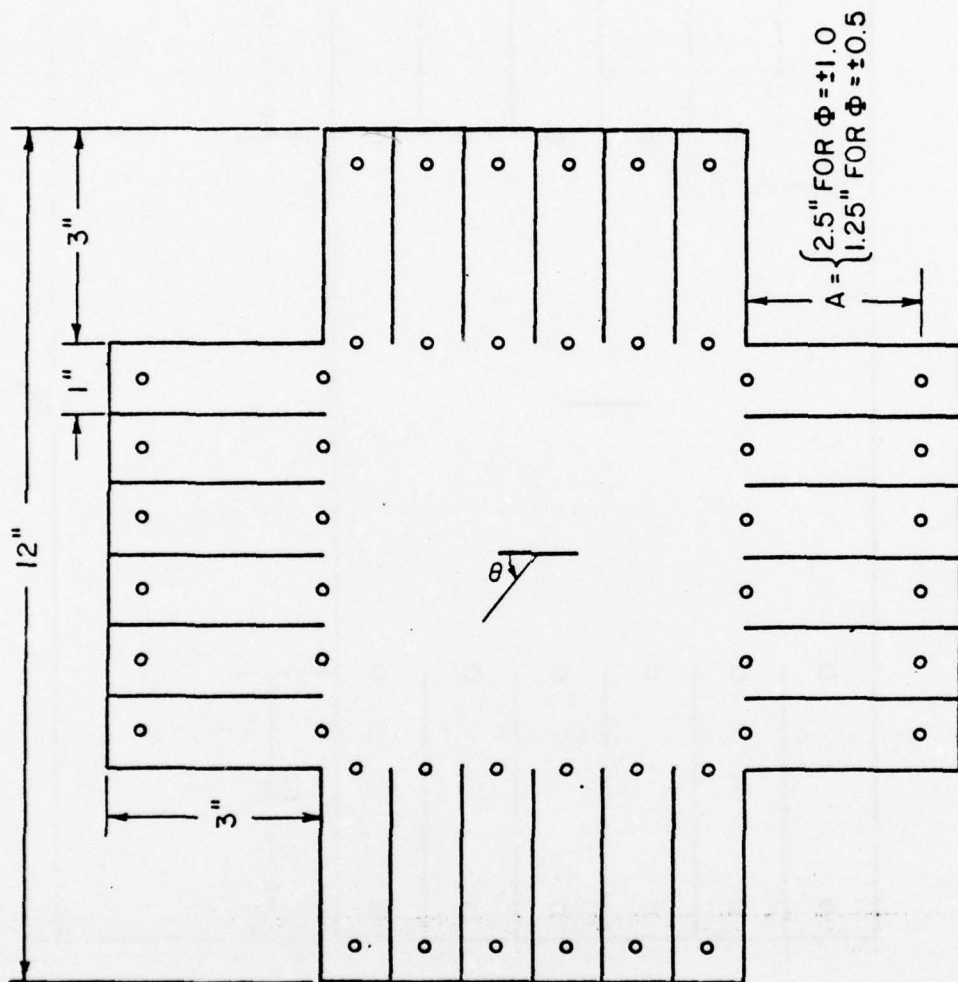


Figure 3.3. Specimen configuration for $\Phi = +1.0$, $+0.5$, -0.5 , and -1.0 .

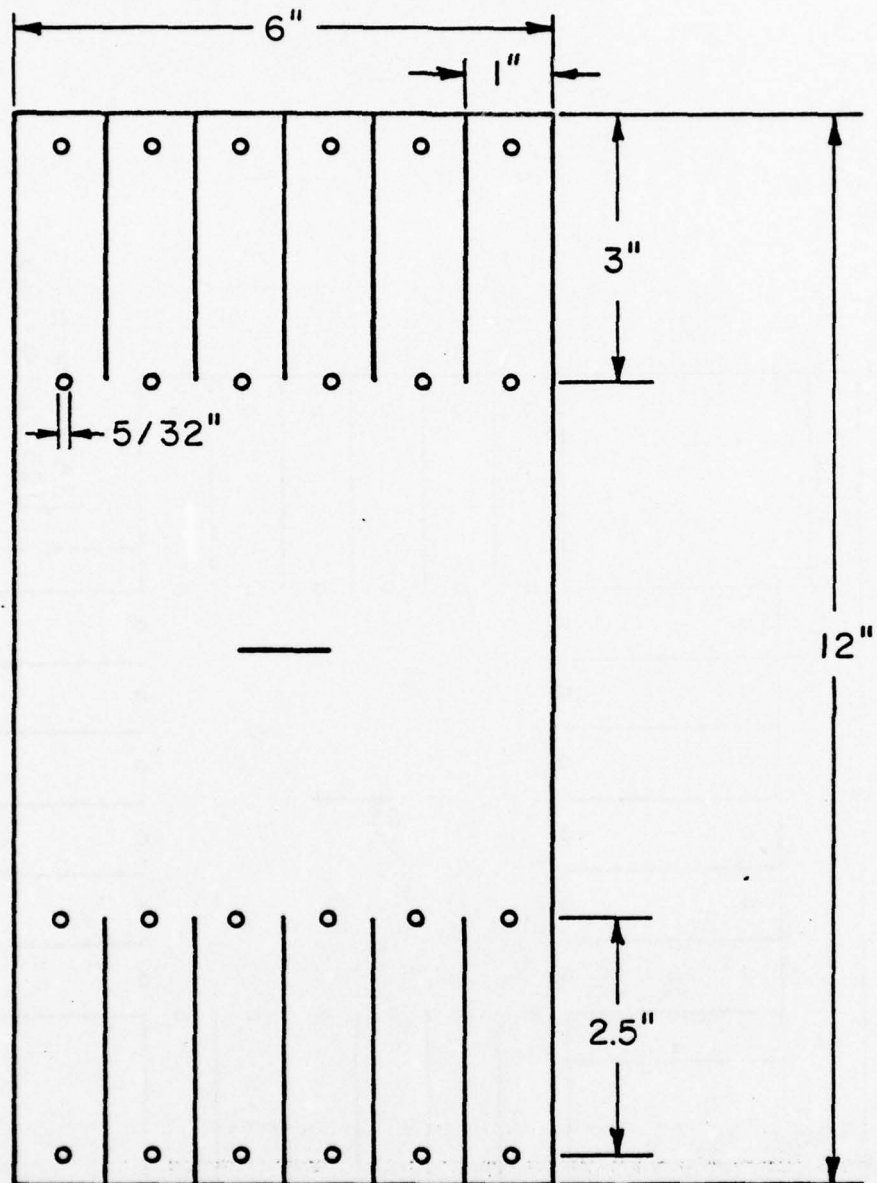


Figure 3.4. Specimen configuration for $\phi = 0.0$.

3.3 Loading Frame

The supporting body of the loading frame was fabricated from 1 in. x 1 in. x 1/8 in. steel angle sections and 1 in. x 1/8 in. steel straps bolted together. The actual loading mechanism is comprised of several parts including the specimen support platform, scissors jack, and loading platform.

The specimen support platform was a 6 in. x 4 in. x 1/4 in. aluminum plate held by two steel rods connected to the loading platform. Its purpose was to support the weight of the model until loads were applied at the critical temperature. At that time, the platform dropped in conjunction with the lowering of the loading platform, allowing the model to be loaded freely. The loading platform supports the weight which is to be applied to the specimen and is lowered by means of the scissors jack.

Loading was achieved through the use of 40 lb. test mono-filament fishing line and ball-bearing fishing swivels. The loading method selected was similar to the one used by Rubayi and Ved⁴⁰ and further expounded upon by Rubayi.⁴¹ The line was threaded through the upper and lower frames as well as the model in a manner illustrated in Figure 3.5, using a continuous length of line on each side of the plate. The swivels were attached to the bottom of the "fingers" by passing 1 inch long, small diameter bars through the eyes. All holes through which the filament passed were

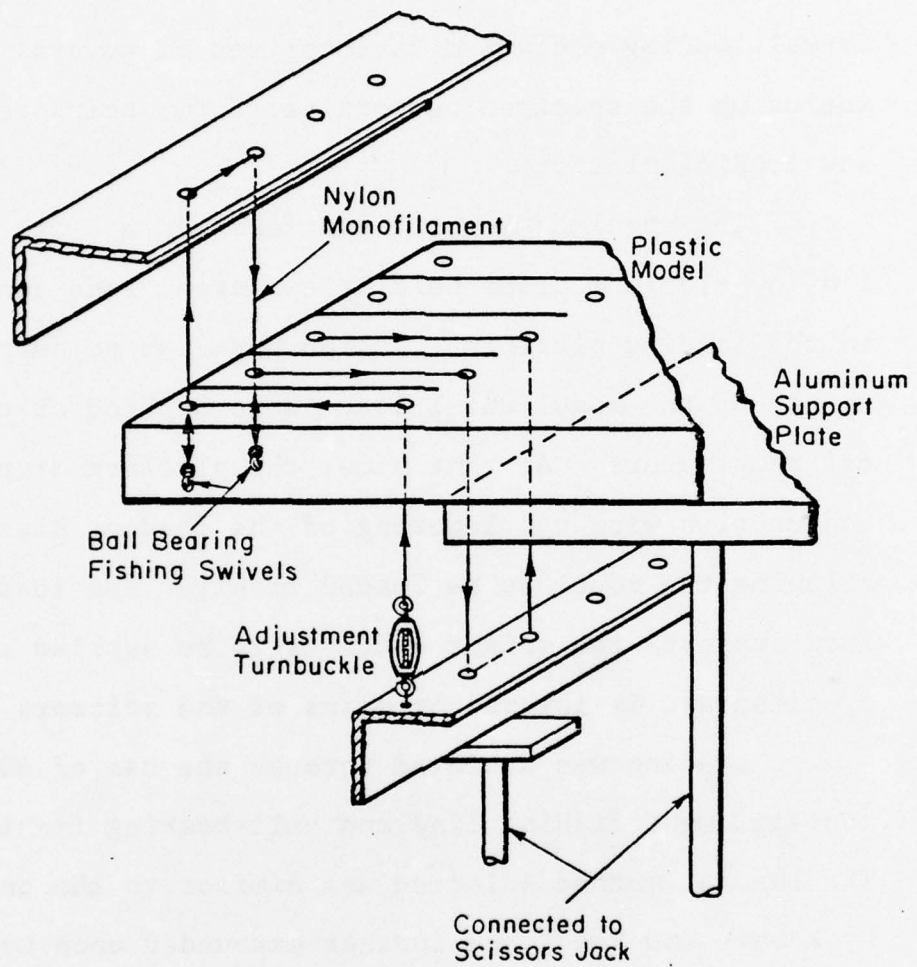


Figure 3.5. Arrangement of loading the model by nylon filament.

shamfered and corners rounded smoothly in order to reduce friction. To further reduce friction and the possibility of twist in the line, all lengths were plucked and the specimen was leveled by adjusting the ends of each line by the use of small turnbuckles fastened to the loading frame.

The calibration beam was suspended from the loading frame and loaded prior to initiation of the stress freezing cycle. Loading was by the four-point bending method. Beam dimensions and load application are illustrated in Figure 3.6.

At this time, the loading frame complete with the unloaded specimen and the loaded calibration beam were placed in the Photolastic P-2307-M oven.

3.4 Stress Freezing Procedure

The stress freezing procedure began with the oven at room temperature. It was increased at a uniform rate of $5^{\circ}\text{F}/\text{hour}$ until the critical temperature of approximately 250°F was attained. The load was applied to the model which was allowed to soak at this temperature for three hours. The temperature was decreased at a rate of $2^{\circ}\text{F}/\text{hour}$ until the oven temperature reached 200°F . From 200°F to 140°F , the rate of temperature decrease was changed to $3^{\circ}\text{F}/\text{hour}$. The temperature was decreased from 140°F at a rate of $5^{\circ}\text{F}/\text{hour}$ until the oven temperature dropped to 100°F . At this point, the oven was shut off and allowed

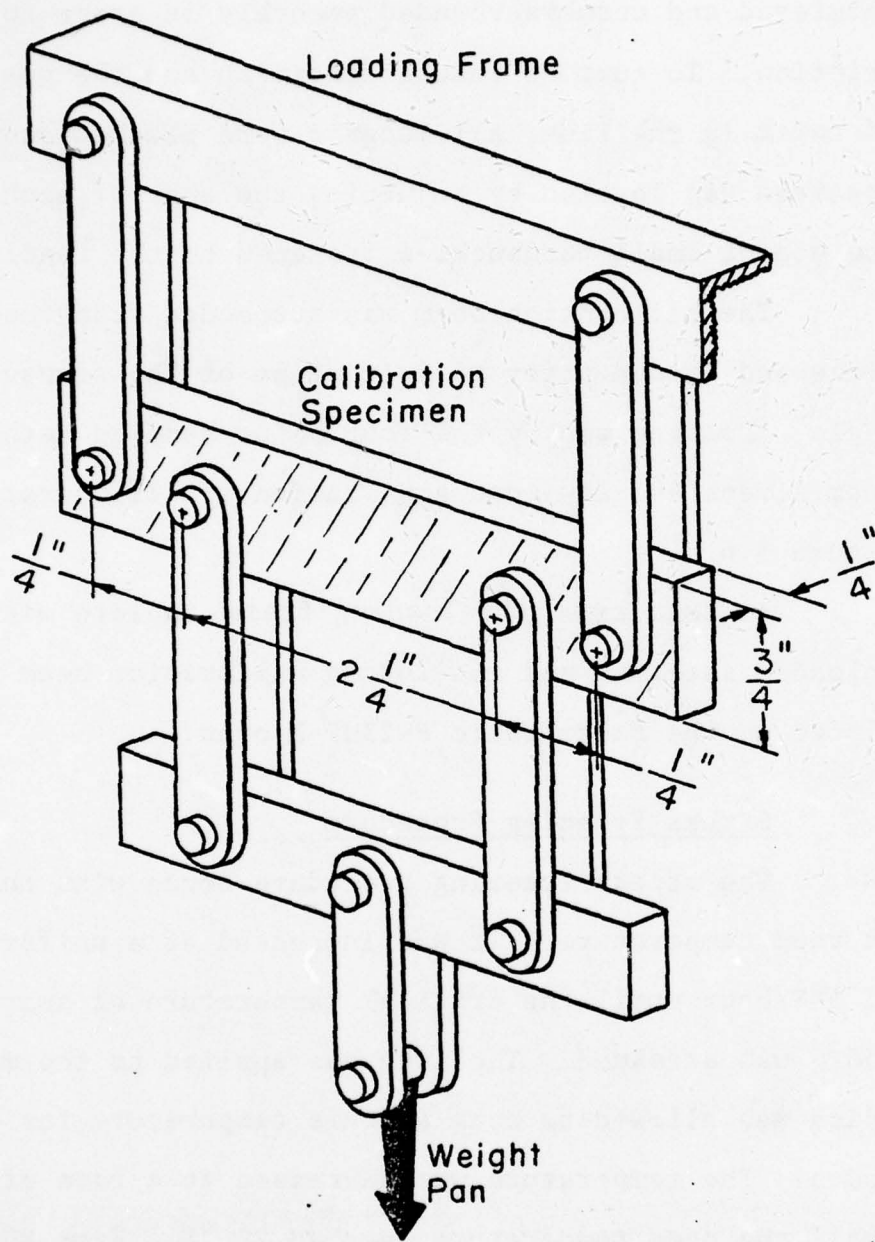


Figure 3.6. Calibration beam and method of loading.

to cool to room temperature. Figure 3.7 is a photograph of the loading frame complete with loaded specimen.

3.5 Slicing Plan and Technique

In order to analyze the three-dimensional stress state in the model but still employ two-dimensional techniques, several slices were removed from the specimen to be analyzed. These slices consisted of a center slice perpendicular to the crack and containing the crack tip at the point of maximum flaw penetration and a surface slice. Figure 3.8 shows the location of these slices with regard to the model. Slice thickness was sufficiently small to allow the effect of strain variation across the thickness to be neglected. Each slice was cut by a thin band saw blade using air-jet cooling. Surfaces were then sanded to a smooth plane.

3.6 Photoelastic Investigation

3.6.1 Calibration Specimen. The stress optical coefficient, f_{σ} , was determined for each specimen by analyzing the calibration beam in a dark and light field circular polariscope. The polariscope used was the modified Columbia polariscope which is described in detail in Appendix A. The calibration beam was placed in the index matching fluid between the partial mirrors of the fringe sharpening and multiplication device described in

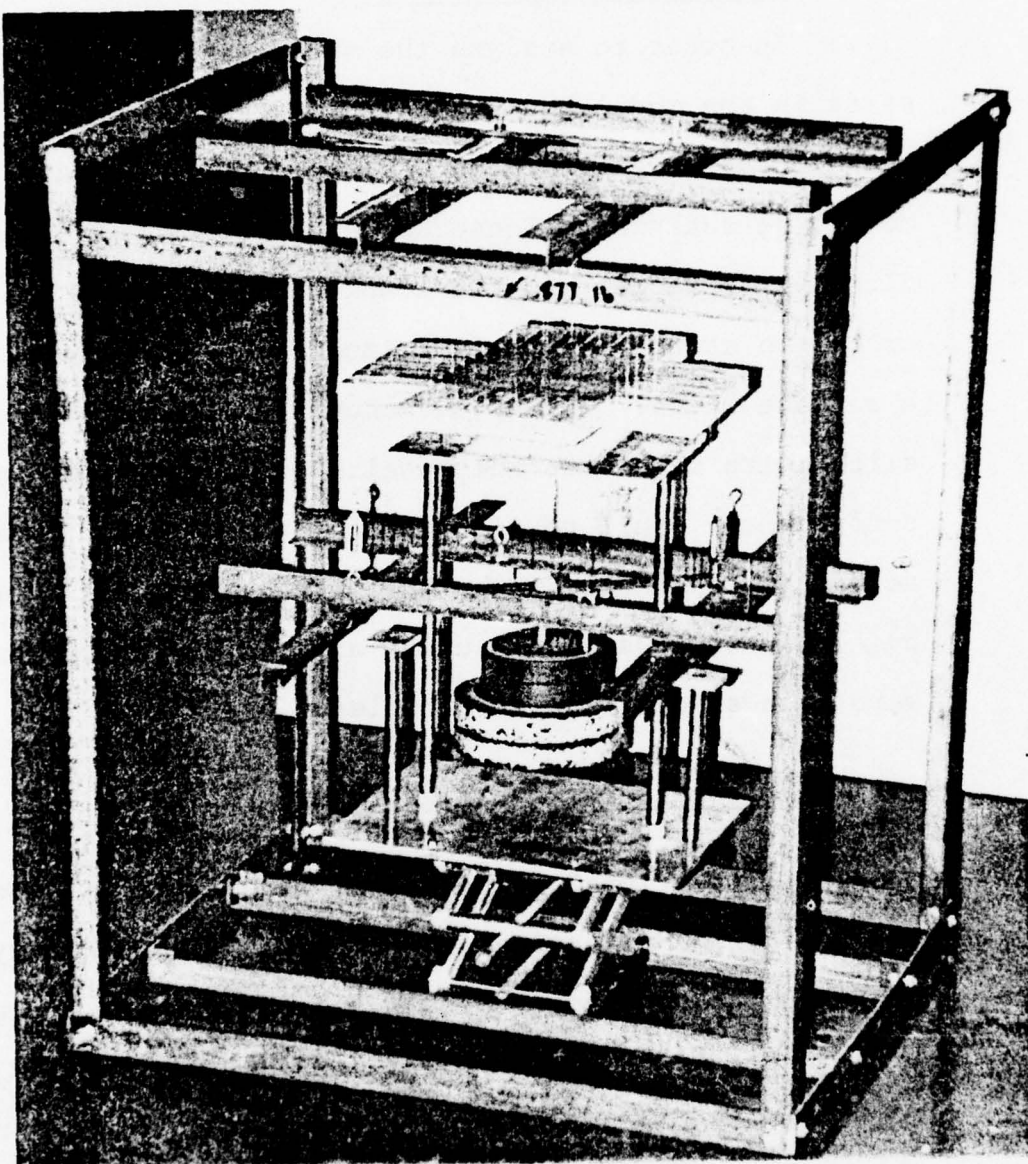


Figure 3.7. Loading frame with a specimen under load.

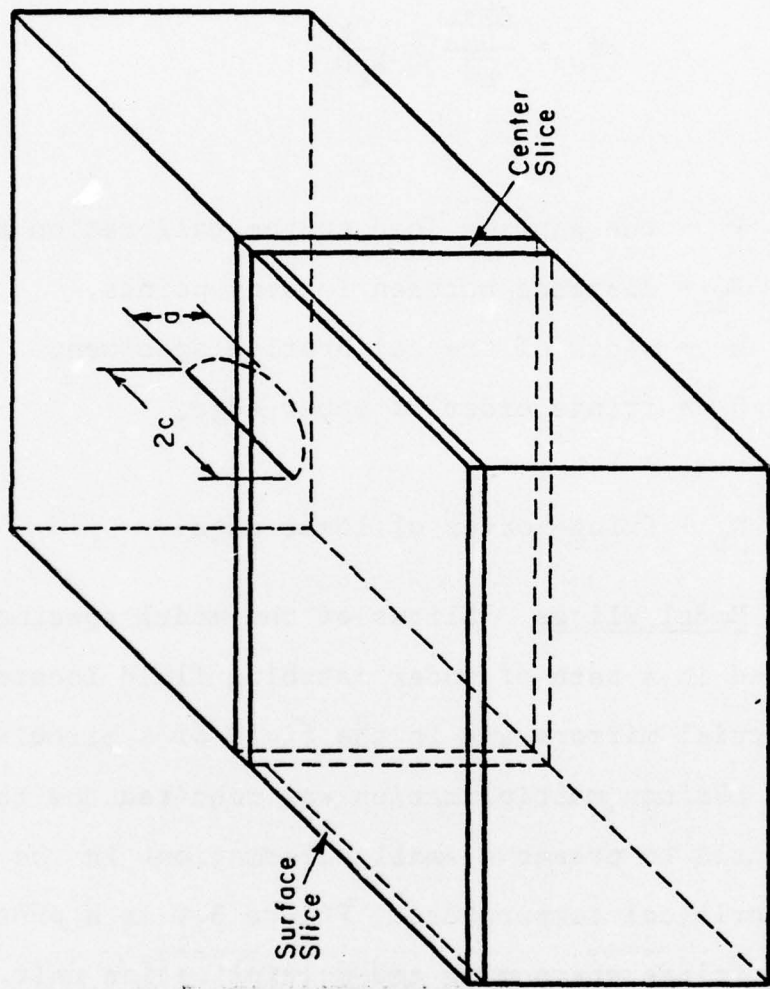


Figure 3.8. Slice locations.

Appendix B. A plot of fringe order versus distance from the neutral axis was constructed to determine exact fringe order at the edges of the calibration beam. The value of f_σ was determined from the equation:

$$f_\sigma = \frac{6P\ell_1}{h^3} \times \frac{h}{N_u N_L} , \quad (3.1)$$

where

P = the applied load to the calibration specimen,

ℓ_1 = distance between loading points,

h = width of the calibration specimen,

N_u = fringe order of upper edge,

and

N_L = fringe order of lower edge.

3.6.2 Model Slices. Slices of the model specimen were immersed in a bath of index matching fluid located between two partial mirrors and in the field of a circular polariscope. Fringe multiplication was required due to the low loads used to preserve small deformations in the material above critical temperature. Figure 3.9 is a photograph of the fringe sharpening and multiplication unit. Photographs were taken of the fringe patterns for fringe sharpening and dark and light field fringe multiplications. The photographs were not used for the measurement of fringe radii, however, as a different approach was employed.

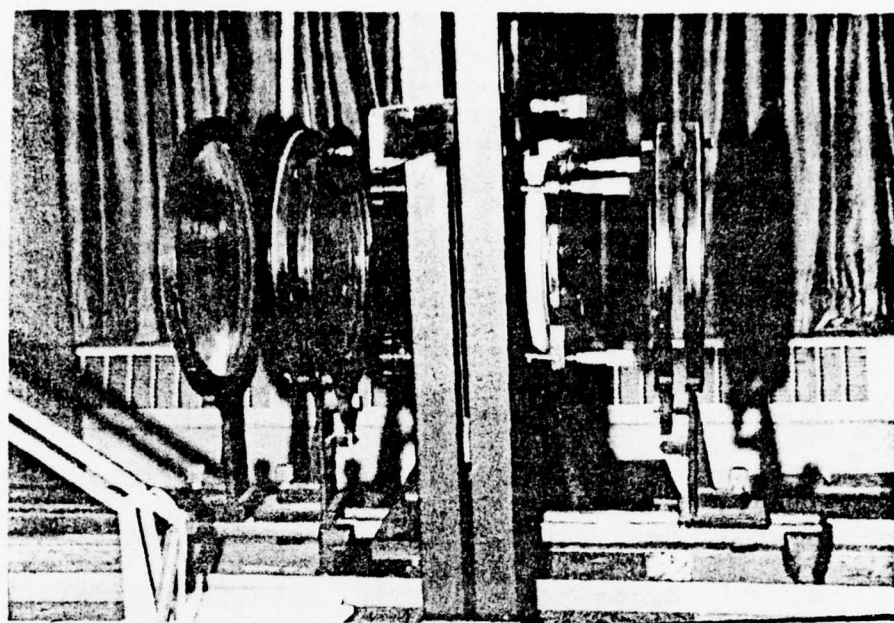


Figure 3.9. Fringe sharpening and multiplication unit.

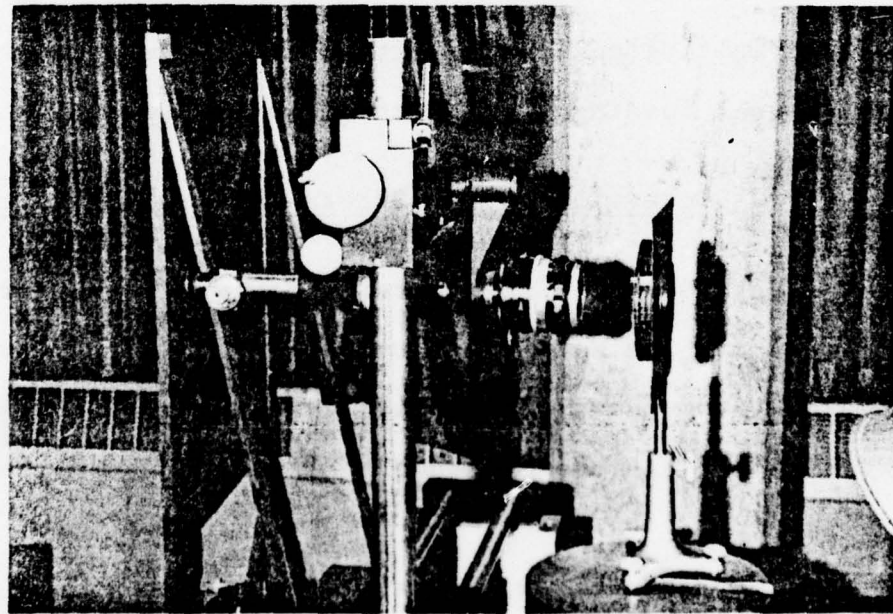


Figure 3.10. Telemicroscope with fringe measuring eyepiece.

Incorporated in the 10X power eyepiece was a movable cross-hair, the lateral travel of which is measured by a series of graduations on the rotating knob. This device can be seen in Figure 3.10. Calibration of the movable cross-hair enabled fringe measurements to be determined directly by visual inspection of model fringe patterns and alleviated the necessity of determining photographic magnification factors. Data were taken from the first series of photographs, however, for comparison with data obtained by the movable cross-hair method. Results suggested that the degree of accuracy of the latter method was equal to that of the photographic method. As a result of these findings, the new approach was utilized for the remainder of the investigation. Typical photographs showing both unmultiplied and multiplied fringe patterns near the crack tip for several loading configurations are shown in Appendix D.

3.7 Determination of Stress Intensity Factors

3.7.1 Mode I. After careful review of the three techniques used for the determination of Mode I stress intensity factors from photoelastic data (see Section 1.4), it was decided to use the method of Schoredl and Smith² outlined below.

Beginning with the stress components in a plane normal to the crack border in the form for Mode I crack

extension suggested by Irwin:

$$\begin{aligned}\sigma_{xx} &= \frac{K_I}{(2\pi r)^{1/2}} \cos\theta (1 - \sin \frac{\theta}{2} \sin \frac{3\theta}{2}) - \sigma_{ox} \\ \sigma_{yy} &= \frac{K_I}{(2\pi r)^{1/2}} \cos^2 \frac{\theta}{2} (1 + \sin \frac{\theta}{2} \sin \frac{3\theta}{2}) \\ \tau_{xy} &= \frac{K_I}{(2\pi r)^{1/2}} \sin \frac{\theta}{2} \cos \frac{\theta}{2} \cos \frac{3\theta}{2}\end{aligned}\quad (3.2)$$

where the notation is given in Figure 3.11. We may substitute Equation (3.2) into

$$\tau_{max}^2 = \frac{1}{4} \{ (\sigma_{xx} - \sigma_{yy})^2 + 4\tau_{xy}^2 \}, \quad (3.3)$$

and evaluate τ_{max}^2 along the line $\theta = \frac{\pi}{2}$ to yield:

$$\tau_{max}^2 = \frac{K_I^2}{8\pi r} + \frac{K_I \sigma_{ox}}{(2\pi r)^{1/2}} + \frac{\sigma_{ox}^2}{4}, \quad (3.4)$$

which may be combined with the stress-optic law resulting in:

$$\frac{n^2 f_r^2}{t^2} = \frac{K_I^2}{2\pi r} + \frac{K_I \sigma_{ox}}{(2\pi r)^{1/2}} + \frac{\sigma_{ox}^2}{4}. \quad (3.5)$$

Solving Equation (3.5) for K_I by use of the quadratic formula gives a positive root of:

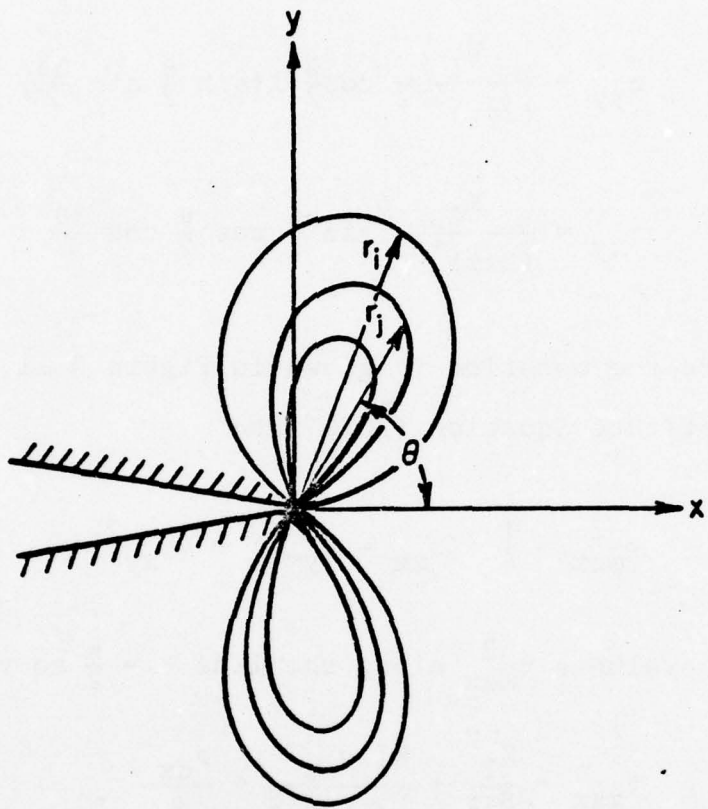


Figure 3.11. Schematic drawing of typical fringe pattern with sign convention and nomenclature.

$$K_I = (\pi r)^{1/2} \left[\left(\frac{2n^2 f \sigma}{t^2} - \sigma_{ox}^2 \right)^{1/2} - \sigma_{ox} \right]. \quad (3.6)$$

Smith simplified Equation (3.6) by neglecting σ_{ox}^2 relative to $\frac{2n^2 f \sigma}{t^2}$ to obtain:

$$K_I = (\pi r)^{1/2} \left[(2)^{1/2} \left(\frac{n f \sigma}{t} \right) - \sigma_{ox} \right]. \quad (3.7)$$

K_I and σ_{ox} can be uncoupled by taking the difference between Equation (3.7) for the i^{th} and j^{th} fringe loops.

Equation (3.8) is the result of this operation:

$$K_I = (2\pi r_i)^{1/2} \frac{f \sigma}{t} \left[\frac{(n_i - n_j)}{1 - \left(\frac{r_i}{r_j} \right)^{1/2}} \right]. \quad (3.8)$$

K_I is computed from Equation (3.8) for all possible permutations of pairs of fringe loops. The average and standard deviation of these values of K_I are determined.

K_I average is recomputed after eliminating values of K_I which fall outside \pm one standard deviation.

Solving Equation (3.5) for σ_{ox} by use of the quadratic formula gives a "positive" root of:

$$\sigma_{ox} = \frac{-K_I}{2(\pi r)^{1/2}} + \left(\frac{n^2 f_\sigma^2}{t^2} - \frac{K_I^2}{4\pi r} \right)^{1/2} \quad (3.9)$$

Using the average K_I computed by the method described previously, values of σ_{ox} are determined for each set of (n, r) data. The same analysis performed in determining an average K_I value is used to determine an average value for σ_{ox} . An example of the computer printout for this operation is shown in Table 3.3.

3.7.2 Mode II. Following in the manner of Irwin,⁴ the stress field in a plane normal to the crack border in the form for Mode II crack extension is:

$$\begin{aligned} \sigma_{xx} &= \frac{-K_{II}}{(2\pi r)^{1/2}} \sin \frac{\theta}{2} [2 + \cos \frac{\theta}{2} \cos \frac{2\theta}{2}] \\ \sigma_{yy} &= \frac{K_{II}}{(2\pi r)^{1/2}} \sin \frac{\theta}{2} \cos \frac{\theta}{2} \cos \frac{3\theta}{2} \\ \tau_{xy} &= \frac{K_{II}}{(2\pi r)^{1/2}} \cos \frac{\theta}{2} [1 - \sin \frac{\theta}{2} \sin \frac{3\theta}{2}] \end{aligned} \quad (3.10)$$

where the notation is given in Figure 3.11. If all measurements of r are taken at $\theta = 0^\circ$, Equation (3.10) reduces to:

Table 3.3. Sample Printout of K_I Values

Crack Angle = 45.0 Degrees
 Biaxiality Ratio = 1.0
 Alpha = 0.0 Degrees
 Stress Fringe Coef. = 2.34
 Slice Thickness = .0530

F(I)	F(J)	R(I)	R(J)	SIF
1.50000	1.33333	.00830	.01390	7.39430
1.50000	1.66667	.00830	.02040	9.28035
1.50000	1.00000	.00830	.03780	9.48657
1.50000	0.83333	.00830	.08510	9.77421
1.33333	1.16667	.01390	.02040	12.45822
1.33333	1.00000	.01390	.03780	11.04994
1.33333	0.83333	.01390	.08510	10.34889
1.16667	1.00000	.02040	.03780	9.92777
1.16667	0.83333	.02040	.08510	10.32358
1.00000	0.83333	.03780	.08510	10.75225
1.50000	1.33333	.00850	.01220	10.28773
1.50000	1.16667	.00850	.02000	9.77091
1.50000	1.00000	.00850	.03970	9.49522
1.50000	0.83333	.00850	.09430	9.72063
1.33333	1.16667	.01220	.02000	9.30350
1.33333	1.00000	.01220	.03970	9.14305
1.33333	0.83333	.01220	.09430	9.54524
1.16667	1.00000	.02000	.03970	8.98804
1.16667	0.83333	.02000	.09430	9.67088
1.00000	0.83333	.03970	.09430	10.48600
<hr/>				
Original N	= 20			
First Avg. SIF	= 9.88936			
Standard Deviation	= 1.00898			
New N	= 16			
New Avg. SIF	= 9.74599			
Standard Deviation	= .49799			

Table 3.3. (Continued)

Crack Angle = 45.0 Degrees
 Biaxiality Ratio = 1.0
 Alpha = 0.0 Degrees
 Stress Fringe Coef. = 2.34
 Slice Thickness = .0530

F(I)	F(J)	R(I)	R(J)	SIF
1.50000	1.33333	.00830	.01390	7.39430
1.50000	1.16667	.00830	.02040	9.28035
1.50000	1.00000	.00830	.03780	9.48657
1.50000	0.83333	.00830	.08510	9.77421
1.33333	1.16667	.01390	.02040	12.45822
1.33333	1.00000	.01390	.03780	11.04994
1.33333	0.83333	.01390	.08510	10.94889
1.16667	1.00000	.02040	.03780	9.92777
1.16667	0.83333	.02040	.08510	10.32358
1.00000	0.83333	.03780	.08510	10.75225
1.50000	1.33333	.00850	.01220	10.28773
1.50000	1.16667	.00850	.02000	9.77091
1.50000	1.00000	.00850	.03970	9.49522
1.50000	0.83333	.00850	.09430	9.72063
1.33333	1.16667	.01220	.02000	9.30350
1.33333	1.00000	.01220	.03970	9.14305
1.33333	0.83333	.01220	.09430	9.54524
1.16667	1.00000	.02000	.03970	8.98804
1.16667	0.83333	.02000	.09430	9.67088
1.00000	0.83333	.03970	.09430	10.46600

Original N = 20
 First Avg. SIF = 9.88936
 Standard Deviation = 1.00898
 New N = 16
 New Avg. SIF = 9.74599
 Standard Deviation = .49799

$$\sigma_{xx} = 0, \sigma_{yy} = 0 \quad (3.11)$$

$$\tau_{xy} = \frac{K_{II}}{(2\pi r)^{1/2}}$$

Substitution of Equation (3.11) into Equation (3.3) yields:

$$\tau_{max}^2 = \frac{K_{II}^2}{2\pi r} \quad (3.12)$$

which may be combined with the stress-optic law to yield:

$$\frac{n^2 f_\sigma^2}{4t^2} = \frac{K_{II}^2}{2\pi r} \quad (3.13)$$

Solution of Equation (3.13) for K_{II} gives:

$$K_{II} = (2\pi r)^{1/2} \frac{nf_\sigma}{2t} \quad (3.14)$$

Values of K_{II} were computed for each set of "n" and "r" data. These values of the stress intensity factor were used in a least squares regression analysis to determine K_{II} at the crack tip (i.e., $r = 0$).

3.7.3 Mixed-Mode. For a crack loaded in both Mode I and Mode II, Paris and Sih⁴² give the stress field in the vicinity of the crack tip as:

$$\begin{aligned}\sigma_{xx} &= \frac{K_I}{(2\pi r)^{1/2}} \cos \frac{\theta}{2} [1 - \sin \frac{\theta}{2} \sin \frac{3\theta}{2}] - \frac{K_{II}}{(2\pi r)^{1/2}} \sin \frac{\theta}{2} \\ &\quad [2 + \cos - \cos \frac{3\theta}{2}] \\ \sigma_{yy} &= \frac{K_I}{(2\pi r)^{1/2}} \cos \frac{\theta}{2} [1 + \sin \frac{\theta}{2} \sin \frac{3\theta}{2}] + \frac{K_{II}}{(2\pi r)^{1/2}} \\ &\quad \sin \frac{\theta}{2} \cos \frac{\theta}{2} \cos \frac{3\theta}{2}\end{aligned}\tag{3.15}$$

$$\begin{aligned}\tau_{xy} &= \frac{K_I}{(2\pi r)^{1/2}} \sin \frac{\theta}{2} \cos \frac{\theta}{2} \cos \frac{\theta}{2} + \frac{K_{II}}{(2\pi r)^{1/2}} \cos \frac{\theta}{2} \\ &\quad [1 - \sin \frac{\theta}{2} \sin \frac{3\theta}{2}]\end{aligned}$$

Substitution of these equations into Equation 3.3 yields the following equation for the maximum in-plane shear stress:

$$\tau_{max} = \frac{1}{2(2\pi r)^{1/2}} \left\{ [K_I \sin \theta + 2K_{II} \cos \theta]^2 + [K_2 \sin \theta]^2 \right\}^{1/2}\tag{3.16}$$

A sketch of the isochromatics in Figure 3.12 reveals that the loops for the case of mixed-mode loading have the same shape as the Mode I fringes, except that they are now centered about a line which is at some angle θ_m to the crack axis. For a given value of r , this angle denotes the line along which τ_m has a maximum value. Smith

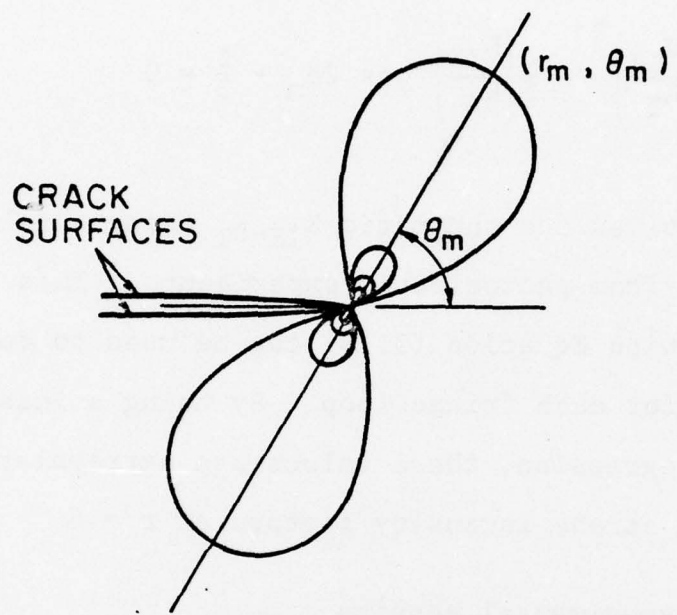


Figure 3.12. Sketch of isochromatics at the crack tip for the mixed-mode problem.

and Smith,³ using a method suggested by Irwin, set $2\tau_m/2\theta = 0$, which in conjunction with Equation (3.16) determines the angle θ_m , where τ_m has a maximum value. The resulting equation:

$$\left(\frac{K_{II}}{K_I}\right)^2 - \frac{4}{3}\left(\frac{K_{II}}{K_I}\right) \cos 2\theta_m - \frac{1}{3} = 0 \quad (3.17)$$

can be solved for the ratio K_{II}/K_I using a value of θ_m measured from photoelastic experiments. This ratio coupled with Equation (3.16) can be used to determine K_I and K_{II} for each fringe loop. By using a least squares linear regression, these values are extrapolated to determine the stress intensity factors at $r = 0$.

3.8 Experimental Results

The results of this investigation can be best presented in two separate sections. Case I will discuss the results obtained for the five specimens with the crack oriented at $\theta = 0$ degrees, while Case II will deal with the three specimens having $\theta = 45$ degrees.

3.8.1 Case I. Table 3.4 presents a summary of specimen details for the five plates in this category. A graphical presentation of the K_I values for $\alpha = 90$ degrees is shown in Figure 3.13, where normalized values of the Mode I stress intensity factors are plotted versus the biaxiality

Table 3.4. Slice Details for $\theta = 0$ Degree Specimens

Specimen No.	Φ	α Degrees	Slice Thickness (in.)	Crack Length (in.)	σ_b psi	K_I $\text{psi}^{\sqrt{\text{in.}}}$	σ_{ox} psi
1	0.0	0	0.041	1.090	0.296	23.172	0.053
1	0.0	90	0.048	1.090	0.296	23.172	12.085
2	+1.0	0	0.054	1.115	0.346	21.120	7.729
2	+1.0	90	0.057	1.115	0.346	21.120	17.542
3	-1.0	0	0.058	1.120	0.340	20.781	2.535
3	-1.0	90	0.059	1.120	0.340	20.781	7.472
6	-0.5	0	0.049	1.122	0.319	28.356	5.906
6	-0.5	90	0.052	1.122	0.319	28.356	8.805
6	-0.5	90	0.057	1.117	0.331	25.808	7.729
7	+0.5	0	0.064	1.117	0.331	25.808	15.689
7	+0.5	90	0.039	1.117	0.331	25.808	0.731

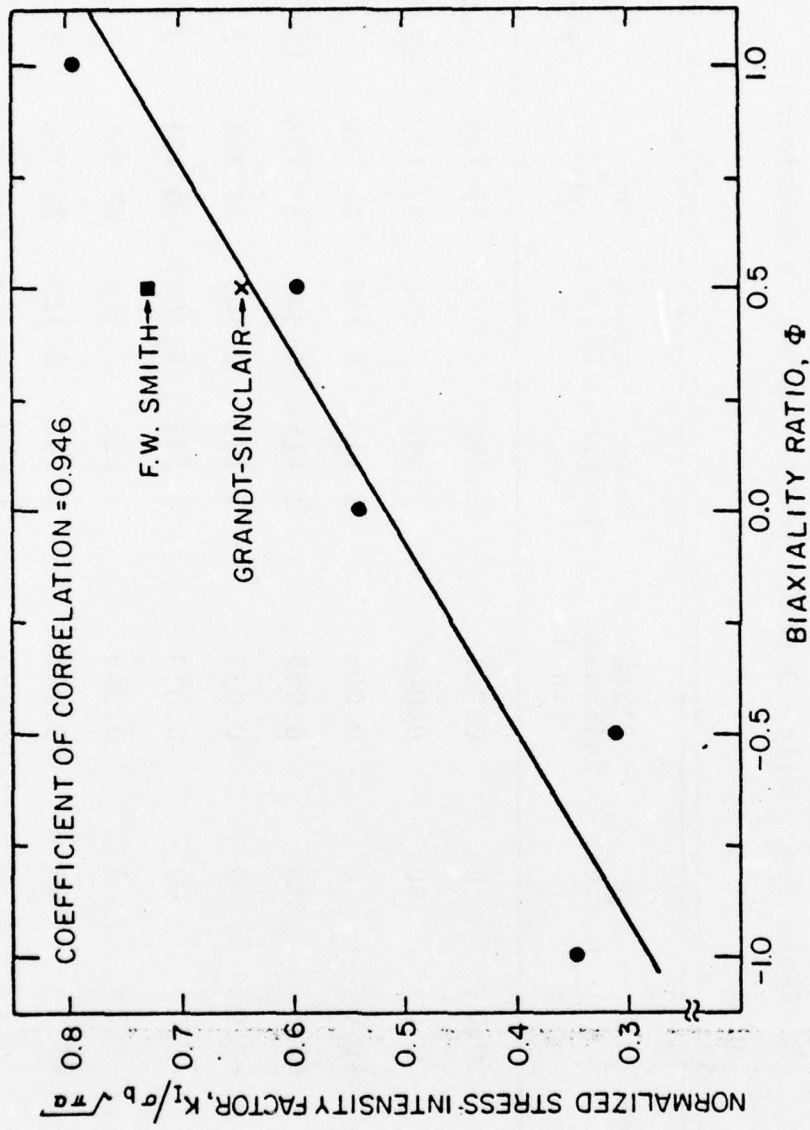


Figure 3.13. Normalized Mode I stress intensity factor versus biaxiality ratio for $\alpha = 90$ degrees.

ratio, ϕ . The line drawn through the points was determined by a least squares linear regression analysis. The coefficient of correlation which was calculated (+0.946) illustrates the presence of a very significant trend. It suggests that a positive biaxiality ratio, as compared to uniaxial bending, shows an increase in Mode I stress intensity factor with increase in biaxiality. Conversely, a negative biaxiality ratio results in a decrease in K_I with increase in biaxiality. A similar trend is recognized in Figure 3.14 for $\alpha = 0$ degrees with the exception of the unexplained deviation at uniaxial bending (i.e., $\phi = 0.0$). The fact that the same trend is observed for both $\alpha = 90$ and 0 degrees solidifies the findings. Theoretical comparison is available only at $\phi = \pm 0.5$ which is cylindrical bending for this material because of the value $v = 0.5$ at the critical temperature. For the slice containing $\alpha = 90$ degrees, comparison is made with the theories presented by F. W. Smith¹⁰ and Grandt and Sinclair.¹⁸ Actual comparison of the theoretical values is shown in Appendix C. The Grandt-Sinclair theoretical point falls on the linear regression line and the Smith theory predicts a value approximately 14 percent higher. This close agreement with the experimentally determined value lends validity to the remaining points. At $\alpha = 0$ degrees, the Smith theory estimate of K_I proved to be 20 percent higher than the experimentally determined curve.

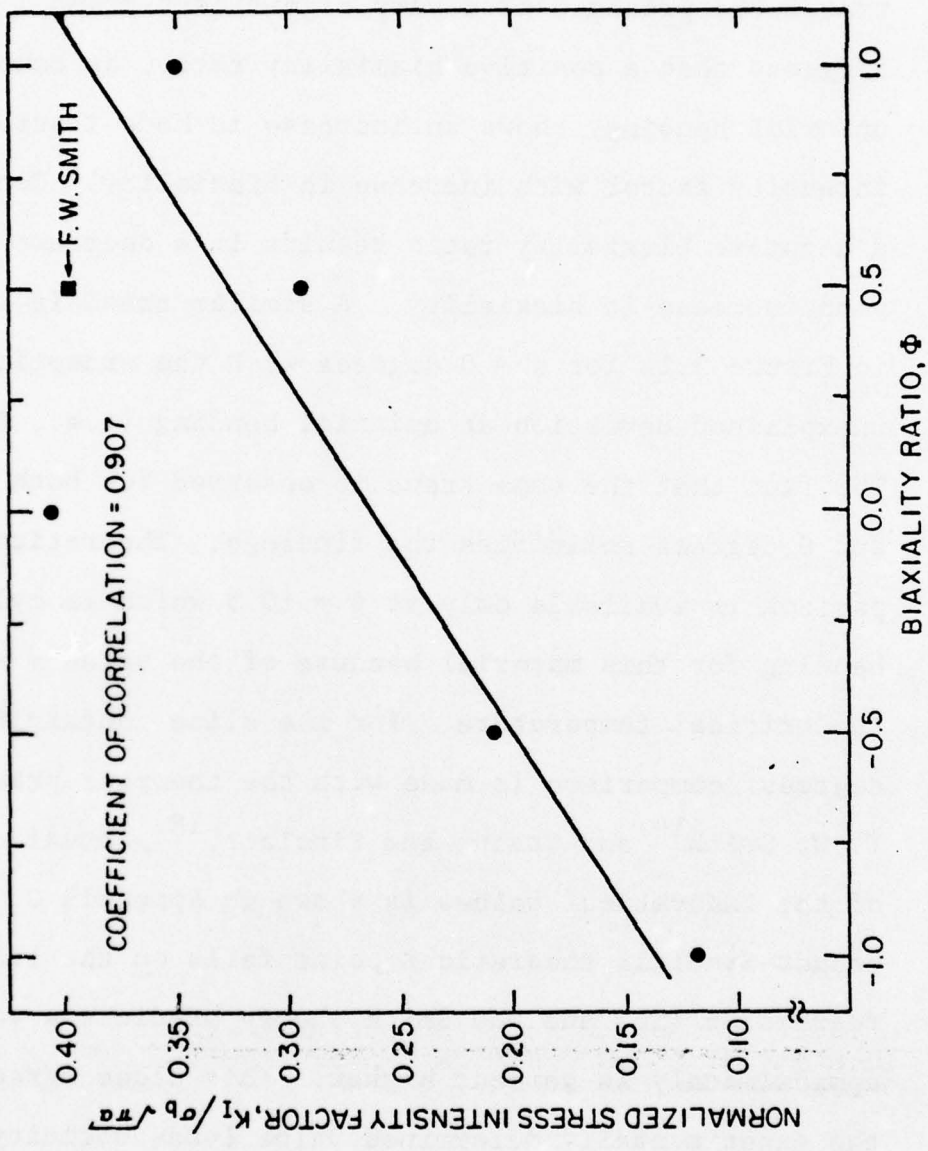


Figure 3.14. Normalized Mode I stress intensity factor versus biaxiality ratio for $\alpha = 0$ degrees.

A qualitative check of the accuracy of the loading can be made by a visual inspection of the isochromatic fringe pattern. Eftis, Subramonian, and Liebowitz⁴³ illustrated the effect of various biaxial loadings on the tilt of the characteristic loops. A symmetric loop occurs only for equal biaxial tension-tension loading, while uniaxial and negative biaxial loadings cause a forward tilt of the loops. For the experiments conducted here, the $\phi = 0.0$ and -1.0 specimen results illustrated forward tilts, while for $\phi = +1.0$ a small backward tilt was observed. Therefore, it can be said that the loading mechanism chosen did introduce relatively accurate loads.

Figure 3.15 is a plot of the normalized remote stress parallel to the crack, σ_{ox} , versus the biaxiality ratio, ϕ , for horizontal slices. The term "remote stress" is somewhat of a misnomer as $-\sigma_{ox}$ is actually a correction factor which must be added to σ_{xx} in order to apply Westergaard's stress function for infinite plates to the solution of finite plate problems. The theoretical value of σ_{ox} can be presented in the form:

$$\sigma_{ox} = (1 - \phi) \frac{6M}{t^2}, \quad (3.18)$$

where

ϕ = biaxiality ratio,

M_o = applied bending moment,

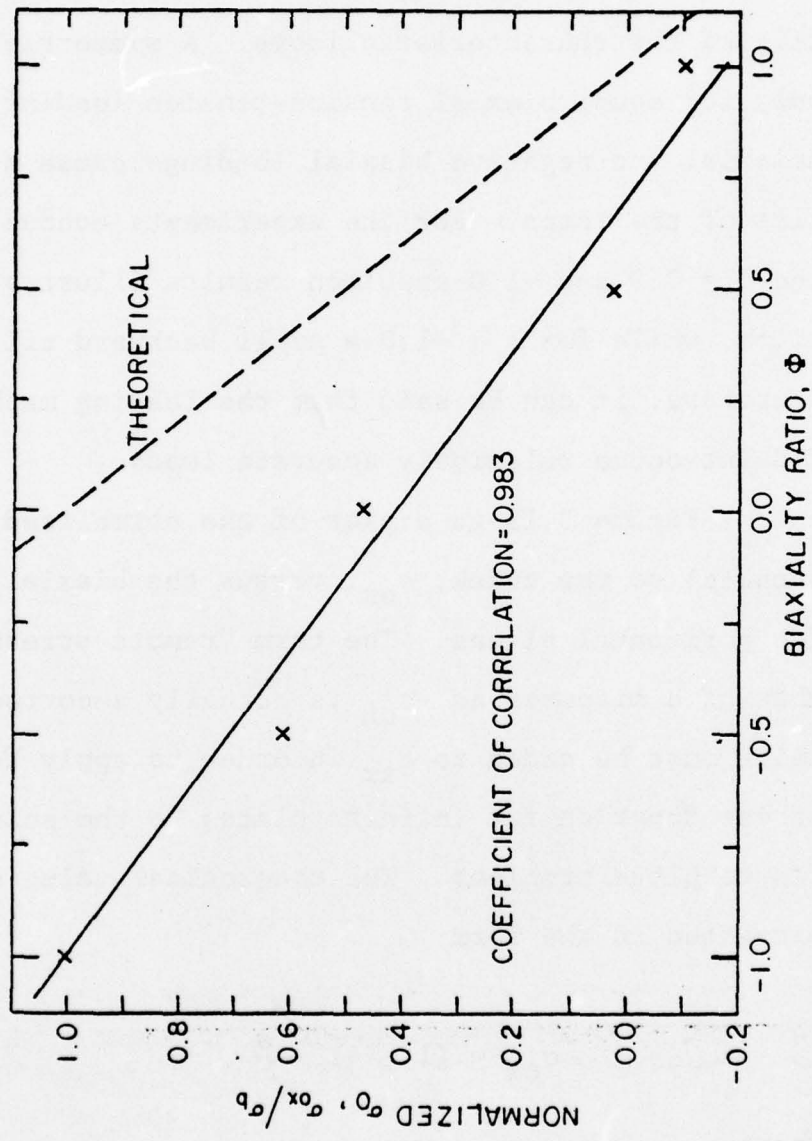


Figure 3.15. Normalized remote stress versus biaxiality ratio for
 $\alpha = 90$ degrees.

t = plate thickness,

and

$$\frac{6M_o}{t^2} = \text{bending stress, } \sigma_b.$$

A partial plot of this equation is represented as a dashed line in Figure 3.15. A comparison between the theoretical values and the measured experimental values reveals that, although the same trend exists, experimental values conform more to the equation:

$$\sigma_{ox} = v(1 - \phi) \frac{6M_o}{t^2}. \quad (3.19)$$

No explanation is given here for this behavior. What should be emphasized is that the trend was reproduced by the experiments. No calculations were made of σ_{ox} for vertical slice, i.e., $\alpha = 0$ degrees.

3.8.2 Case II. Three specimens had semi-elliptical surface flaws which were oriented at 45 degrees to the direction of the applied moments. Specimen details are compiled in Table 3.5.

The uniaxial bending test was conducted first. As expected, the surface slice revealed the presence of mixed-mode (I-II) fringes. No fringes could be resolved for the vertical slice even with large orders of fringe multiplication. A combination of Modes I and II was anticipated

at this location. The value of θ_m (see Figure 3.12) was measured and found to be $\theta_m = 23.5$ degrees. Substitution of this value into Equation (3.17) resulted in the equality:

$$K_{II} = 1.47 K_I. \quad (3.20)$$

Values of K_I were determined using Equation (3.16) and plotted versus distance from the crack tip, r . This is illustrated in Figure 3.16. Using a least squares linear regression analysis, a value of K_I was determined at the crack tip, i.e., $r = 0$. The resulting values, as shown in Table 3.5 are:

$$K_I = 9.990 \text{ psi}\sqrt{\text{in}}.$$

$$K_{II} = 14.685 \text{ psi}\sqrt{\text{in}}.$$

Comparison is made between these values and that of $K_I = 12.085 \text{ psi}\sqrt{\text{in}}$. obtained from Specimen No. 1, where $\theta = 0$ degrees. Although the K_I value for $\theta = 45$ degrees is lower, Shah³⁷ found that the presence of K_{II} has a significant effect on the K_I at which fracture occurs.

Equal biaxial tension-tension loading, $\phi = +1.0$, resulted in pure Mode I isochromatic fringe loops. This is what was expected and reaffirmed the belief that the loading frame was performing accurately. The computer program utilized for all Case I studies was implemented for the determination of K_I . Normalized values of

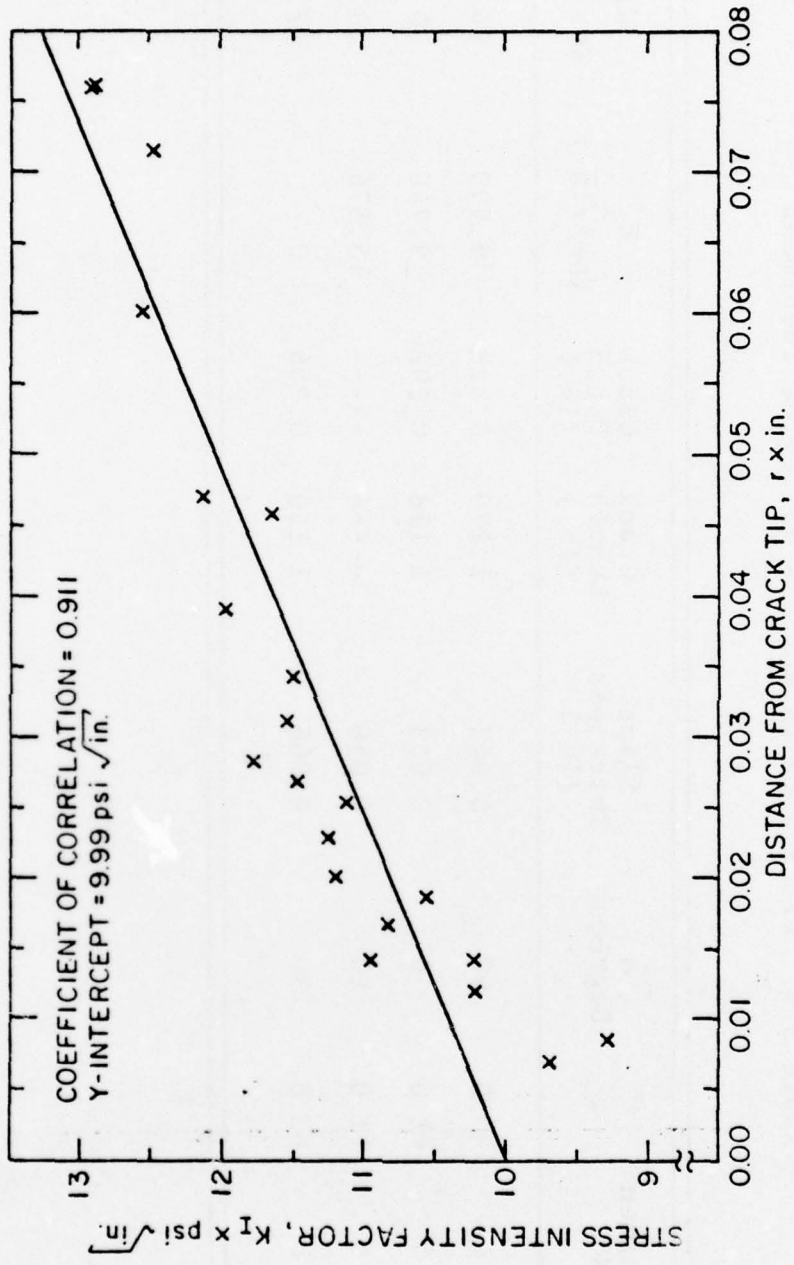


Figure 3.16. Mode I stress intensity factor versus distance from crack tip for $\phi = 0.0$ and $\alpha = 90$ degrees.

Table 3.5. Slice Details for $\theta = 45$ Degree Specimens

Specimen No.	Φ	α Degrees	Slice Thickness (in.)	Crack Length (in.)	Crack Depth (in.)	K_I (psi/in.)	K_{II} (psi/in.)
4	0.0	90	0.042	1.120	0.328	9.990	14.685
5	+1.0	0	0.053	1.118	0.292	9.746	0
5	+1.0	90	0.056	---	---	15.576	0
8	-1.0	90	0.066	1.120	0.346	0	7.92

K_{I_N} = 0.387 at $\alpha = 0$ degrees and K_{I_N} = 0.619 at $\alpha = 90$

degrees were obtained as opposed to K_{I_N} = 0.351 and

K_{I_N} = 0.797, respectively for the $\theta = 0$ degrees test.

This represents a decrease in K_I of 22 percent for the surface slice and an increase in K_I of 10 percent at the base of the crack. Using the higher values for $\alpha = 90$ degrees, it can be noted that the crack oriented at 45 degrees to the loading would not be as critical.

The final specimen tested was a plate containing a crack at 45 degrees to the applied moments and loaded under a negative biaxiality ratio, $\Phi = 1.0$. If the load was accurately applied, it was anticipated that the isochromatic fringes of the surface slice would reveal pure Mode II loading. This is precisely what did occur. Using Equation (3.14) and the procedure described in Section 3.7.2, a value of $K_{II} = 7.92 \text{ psi}\sqrt{\text{in.}}$ was obtained. Figure 3.17 is a plot of K_{II} versus distance from the crack tip and illustrates how this value was determined. A much larger K_{II} was expected due to the value of K_{II} obtained from the $\Phi = 0.0$ specimen. There is a strong possibility that the method of loading used in this investigation does not lend itself to the acquisition of accurate pure Mode II stress intensity factors. However, the mere presence of pure Mode II deformation when anticipated alludes to the accuracy of the method of loading. Isochromatic fringes could not be resolved in the $\alpha = 0$ degrees slice even at high orders of magnification.

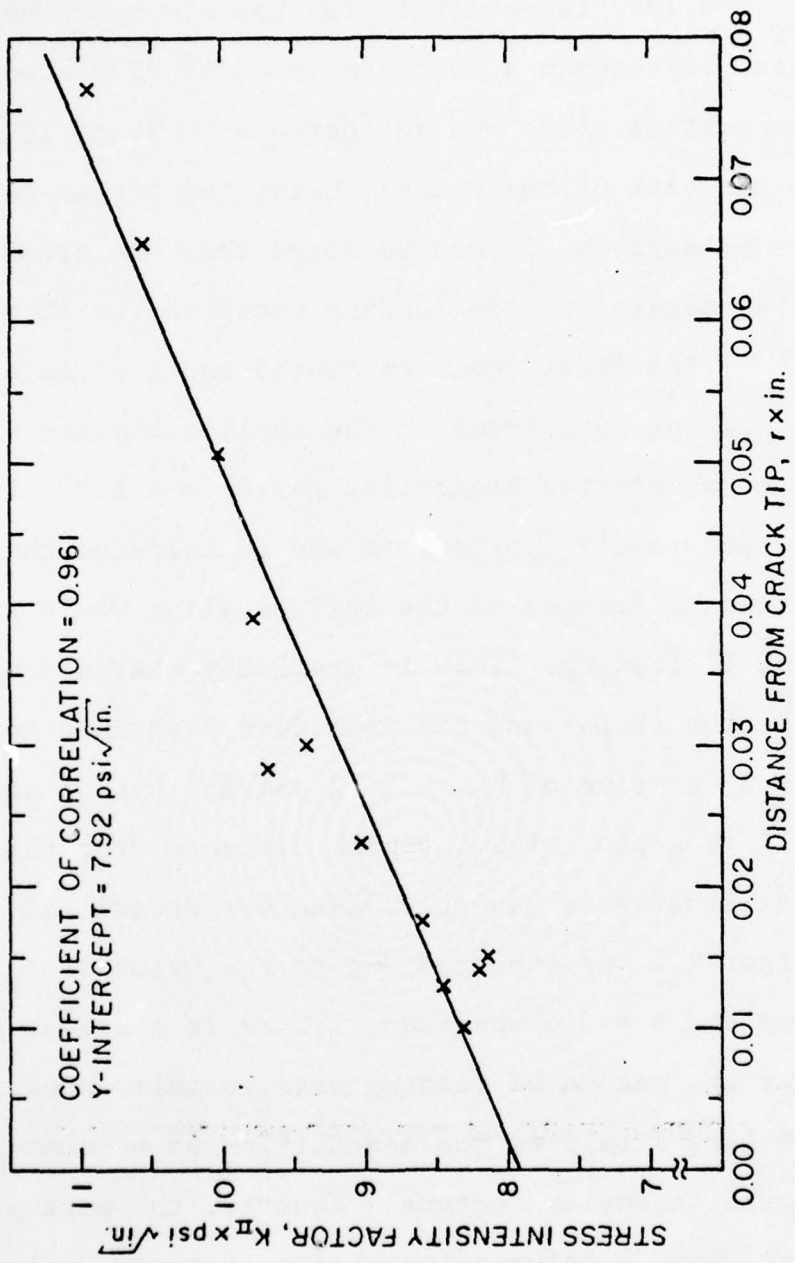


Figure 3.17. Mode II stress intensity factor versus distance from crack tip for $\phi = -1.0$ and $\alpha = 90$ degrees.

CHAPTER IV

SUMMARY AND CONCLUSIONS

4.1 Summary

A series of photoelastic stress-freezing experiments was conducted in an attempt to determine the effect of various biaxial load ratios on the crack-tip stress intensity factors. Plates containing semi-elliptical surface flaws oriented at 0 and 45 degrees to the applied load were subjected to biaxial bending moments ranging from $\phi = +1.0$ to $\phi = -1.0$. Stress intensity factors were experimentally determined at the interface of the crack tip and the plate surface, and the point of maximum flaw penetration.

4.2 Conclusions

Based upon the results of the experimental analysis the following conclusions can be drawn:

1. For cracks oriented at $\theta = 0$ degrees, the ratio of applied biaxial bending moments has a significant effect upon crack-tip stress intensity factor. For both points on the crack tip studied, a positive biaxiality ratio, as compared to uniaxial bending, shows an increase in K_I with increase in biaxiality. Conversely, a negative biaxiality ratio results in a decrease in K_I with increase in biaxiality.

2. The chosen method of loading is capable of applying accurate biaxial bending loads to photoelastic specimens. Quantitative and qualitative comparisons with available theoretical solutions illustrated good agreement.
3. The optical method of obtaining fringe data employed can be used to obtain data with accuracy comparable to photographic techniques.

The photoelastic stress-freezing method has been shown to be a powerful tool in the study of linear elastic fracture mechanics. It is hoped that work will continue to determine an accurate conclusion to the controversial subject addressed in this paper.

BIBLIOGRAPHY

1. Etheridge, J. M. and Dally, J. W., "A Critical Review of Method for Determining Stress-Intensity Factors from Isochromatic Fringes," Experimental Mechanics, Vol. 17, No. 7, July 1977, pp. 248-254.
2. Schroedl, M. A. and Smith, C. W. "Local Stresses Near Deep Surface Flaws Under Cylindrical Bending Fields," Progress in Flaw Growth and Fracture Toughness Testing, ASTM STP 536, American Society for Testing and Materials, 1973, pp. 45-63.
3. Smith, D. G. and Smith, C. W., "Photoelastic Determination of Mixed Mode Stress Intensity Factors," Engineering Fracture Mechanics, Vol. 4, 1972, pp. 357-366.
4. Irwin, G. R., "Analysis of Stresses and Strains Near the End of a Crack Traversing a Plate," Journal of Applied Mechanics, Vol. 24, Transactions of ASME, Series E, Vol. 79, September 1957, pp. 361-364.
5. Griffith, A. A., "The Phenomena of Rupture and Flow in Solids," Philosophical Transactions A, Royal Society of London, Vol. 221, 1921, p. 163.
6. Irwin, G. R., "Crack Extension Force for a Part Through Crack in a Plate," Journal of Applied Mechanics, Vol. 29, No. 4, Transactions of ASME, Series E, Vol. 84, December 1962, pp. 651-654.
7. Green, A. E. and Sneddon, I. N., "The Distribution of Stress in the Neighborhood of a Flat Elliptical Crack in an Elastic Solid," Proceedings of the Cambridge Philosophical Society, Vol. 46, 1950, pp. 159-163.
8. Wigglesworth, L. A., "Stress Distribution in a Notched Plate," Mathematica, Vol. 4, 1947, pp. 76-96.
9. Kobayashi, A. S., "On the Magnification Factors of Deep Surface Flaws," Boeing Structural Research Memorandum, No. 16, December 1965.
10. Smith, F. W., "Stress Intensity Factors for a Semi-Elliptical Surface Flaw," Structural Development and Research Memorandum 17, the Boeing Company, Seattle, Washington, August 1966.

11. Smith, F. W., Emery, A. F., and Kobayashi, A. S., Journal of Applied Mechanics, Vol. 34, Transactions of ASME, Series E, Vol. 89, 1967, pp. 953-959.
12. Smith, F. W. and Alavi, M. J., "Stress Intensity Factors for a Part Circular Surface Flaw," Proceedings of the First International Conference on Pressure Vessel Technology, Delft, The Netherlands, 1969.
13. Kobayashi, A. S. and Moss, W. L., "Stress Intensity Magnification Factors for a Surface-Flawed Tension Plate and a Notched Round Tension Bar," Second International Conference on Fracture, Brighton, England, 1968.
14. Thresher, R. W. and Smith, F. W., "Stress Intensity Factors for a Surface Crack in a Finite Solid," Journal of Applied Mechanics, Transactions of ASME, Vol. 94, March 1972, pp. 195-200.
15. Rice, J. R., and Levy, N., "The Part-Through Surface Crack in an Elastic Plate," Transactions of ASME, Journal of Applied Mechanics, March 1972, pp. 185-194.
16. Shah, R. C. and Kobayashi, A. S., "Stress Intensity Factors for an Elliptical Crack Approaching the Surface of a Semi-Infinite Solid," International Journal of Fracture, Vol. 9, No. 2, June 1973, pp. 133-146.
17. Marrs, G. R. and Smith, C. W., "A Study of Local Stresses Near Surface Flaws in Bending Fields," Stress Analysis and Growth of Cracks, Proceedings of the 1971 National Symposium on Fracture Mechanics, Part I, ASTM STP 513, American Society for Testing Materials, 1972, pp. 22-36.
18. Grandt, A. F., Jr. and Sinclair, G. M., "Stress Intensity Factors for Surface Cracks in Bending," Stress Analysis and Growth of Cracks, Proceedings of the 1971 National Symposium on Fracture Mechanics, Part I, ASTM 513, American Society for Testing and Materials, 1972, pp. 37-58.

19. Shah, R. C. and Kobayashi, A. S., "Stress Intensity Factor for an Elliptical Crack Approaching the Surface of a Plate in Bending," Stress Analysis and Growth of Cracks, Proceedings of the 1971 National Symposium on Fracture Mechanics, Part I, ASTM STP 513, American Society for Testing and Materials, 1972, pp. 3-21.
20. Schroedl, M. A., McGowan, J. J., and Smith, C. W., "Determination of Stress Intensity Factors from Photoelastic Data with Application to Surface Flaw Problems," Journal of Experimental Mechanics, Vol. 14, No. 10, pp. 392-399.
21. Smith, F. W. and Sorenson, D. R., "The Semi-Elliptical Surface Crack -- A Solution by the Alternating Method," International Journal of Fracture, Vol. 12, No. 1, Feb. 1972.
22. Kibler, J. J. and Roberts, R., "The Effect of Biaxial Stresses on Fatigue and Fracture," Journal of Engineering for Industry, Transactions of ASME, Vol. 92, November 1970, pp. 727-734.
23. Adams, N. J. I., "Some Comments on the Effect of Biaxial Stress on Fatigue Crack Growth and Fracture," Engineering Fracture Mechanics, Vol. 5, 1973, p. 983.
24. Radon, J. C., Leever, P. S., and Culver, L. E., "A Simple Testing Technique for Fracture Under Biaxial Stresses," Experimental Mechanics, June 1977, pp. 228-232.
25. Joshi, S. R. and Shewchuk, J., "Fatigue-Crack Propagation in a Biaxial-Stress Field," Experimental Mechanics, Vol. 10, No. 12, 1970, pp. 529-533.
26. Oh, K. P. L., Vardar, O., and Finnie, I., "Failure of Brittle Solids Under Biaxial Stresses," International Journal of Fracture, Vol. 9, 1973, pp. 372-375.
27. Newman, J. C., Jr., "An Improved Method of Collocation for the Stress Analysis of Cracked Plates with Various Shaped Boundaries," NASA TND-6376, August 1971.
28. Grandt, Captain A. F., Jr., "A General Stress Intensity Factor Solution for Thru-Cracked Fastener Holes," International Journal of Fracture, Vol. 11, No. 2, April 1975, pp. 283-294.

29. Hilton, P. D., "Plastic Intensity Factors for Cracked Plates Subjected to Biaxial Loading," International Journal of Fracture, Vol. 9, No. 2, June 1973.
30. Miller, K. J. and Kfouri, A. P., "An Elastic-Plastic Finite Element Analysis of Crack Tip Fields Under Biaxial Loading Conditions," International Journal of Fracture, Vol. 10, No. 3, September 1974, pp. 393-404.
31. Lee, J. D. and Liebowitz, H., "The Nonlinear and Biaxial Effects on Energy Release Rate, J-Integral, and Stress Intensity Factor," Engineering Fracture Mechanics, Vol. 9, 1977, pp. 765-779.
32. Smith, S. H., "Analysis of Energy Quantities for Fracture Under Biaxial Stresses," Presented at Conference on Prospects of Fracture Mechanics, Delft, Netherlands, 1974.
33. Eftis, J., Subramonian, N., and Liebowitz, H., "Biaxial Load Effects on the Crack Border Elastic Strain Energy and Strain Energy Rate," Engineering Fracture Mechanics, Vol. 9, 1977, pp. 753-764.
34. Wilson, W. K., "Combined Mode Fracture Mechanics," Ph.D. Thesis, University of Pittsburgh, 1969.
35. Pook, L. P., "The Effect of Crack Angle on Fracture Toughness," Engineering Fracture Mechanics, Vol. 3, 1971, pp. 205-218.
36. Iida, S. and Kobayashi, A. S., "Crack Propagation Rate in 7075-T6 Plates Under Cyclic Tensile and Transverse Shear Loadings," Journal of Basic Engineering, Transactions of the ASME, Series D, Vol. 91, 1969, pp. 764-769.
37. Shah, R. C., "Fracture Under Combined Modes in 4340 Steel," ASTM STP 560, American Society for Testing and Materials, 1974, pp. 29-52.
38. Gdoutos, E. E. and Theocaris, P. S., "A Photoelastic Determination of Mixed-Mode Stress-Intensity Factors," Experimental Mechanics, Vol. 18, 1978, pp. 87-96.
39. Fichter, W. B., "Stresses at the Tip of a Longitudinal Crack in a Plate Strip," NASA TR R-265, August 1962.

40. Rubayi, N. A. and Ved, R., "Photoelastic Analysis of a Thick Square Plate Containing Central Crack and Loaded by Pure Bending," International Journal of Fracture, Vol. 12, No. 3, June 1976, pp. 435-451.
41. Rubayi, N. A., Personal Communication, February 1977.
42. Paris, P. C. and Sih, G. C., "Stress Analysis of Cracks," ASTM Special Technical Publication No. 381, 1964, p. 30.
43. Eftis, J., Subramonian, N., and Liebowitz, H., "Crack Border Stress and Displacement Equations Revisited," Engineering Fracture Mechanics, Vol. 9, 1977, pp. 189-210.
44. Post, D., "Isochromatic Fringe Sharpening and Fringe Multiplication in Photoelasticity," Proceedings of the S.E.S.A., Vol. 12, No. 2, 1955, pp. 143-156.

APPENDIX A
CONSTRUCTION OF POLARISCOPE

The polariscope used for this investigation necessitated renovation due to the addition of a fringe sharpening and multiplication unit. This device requires a high intensity light source which was not initially present in the system.

The original design consisted of a 100-watt mercury vapor lamp, two 10-inch collimating lenses, two quarter-wave plates, and two rotatable polarizers arranged as shown in Figure A.1. The fringe sharpening and multiplication unit was inserted between the two quarter-wave plates. This device is explained in greater detail in Appendix B. It was concluded that a 250-watt mercury vapor lamp would adequately fulfill the light intensity requirements. Through a series of lenses, the light emitted from the lamp is focused onto a pinhole which is located at the focal point of the collimating lens. To incorporate the addition of the larger lamp and the focusing lenses, the lamp housing was lengthened. The heat generated by the 250-watt lamp necessitated forced air cooling through the use of a small blower directed at the ceramic lamp base. Figure A-2 is a schematic representation of the updated polariscope.

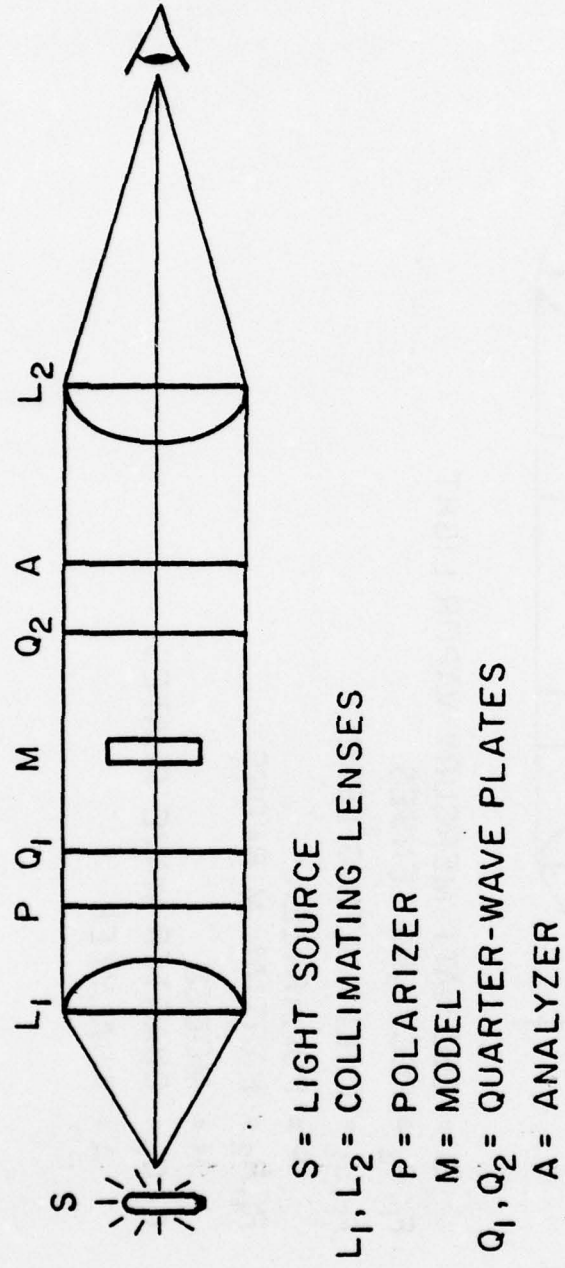


Figure A.1. Arrangement of polariscope components.

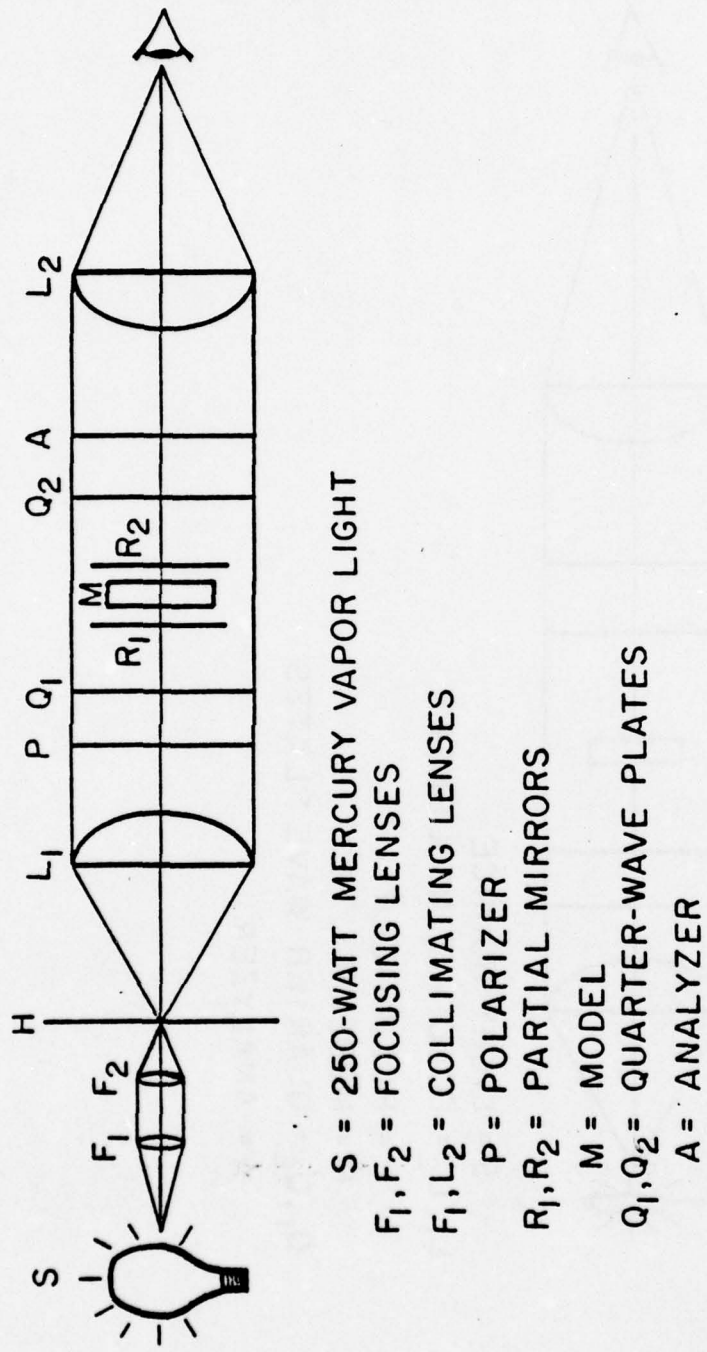


Figure A.2. Arrangement of renovated polariscope.

A telemicroscope with a movable crosshair (described in Section 3.6.2) and a Nikon f1.4 lens was placed at the focal length of the second 10-inch lens. Photographs of fringe patterns were taken through the telescope with a Nikon F camera. Figure A.3 is an overview of the polarscope.

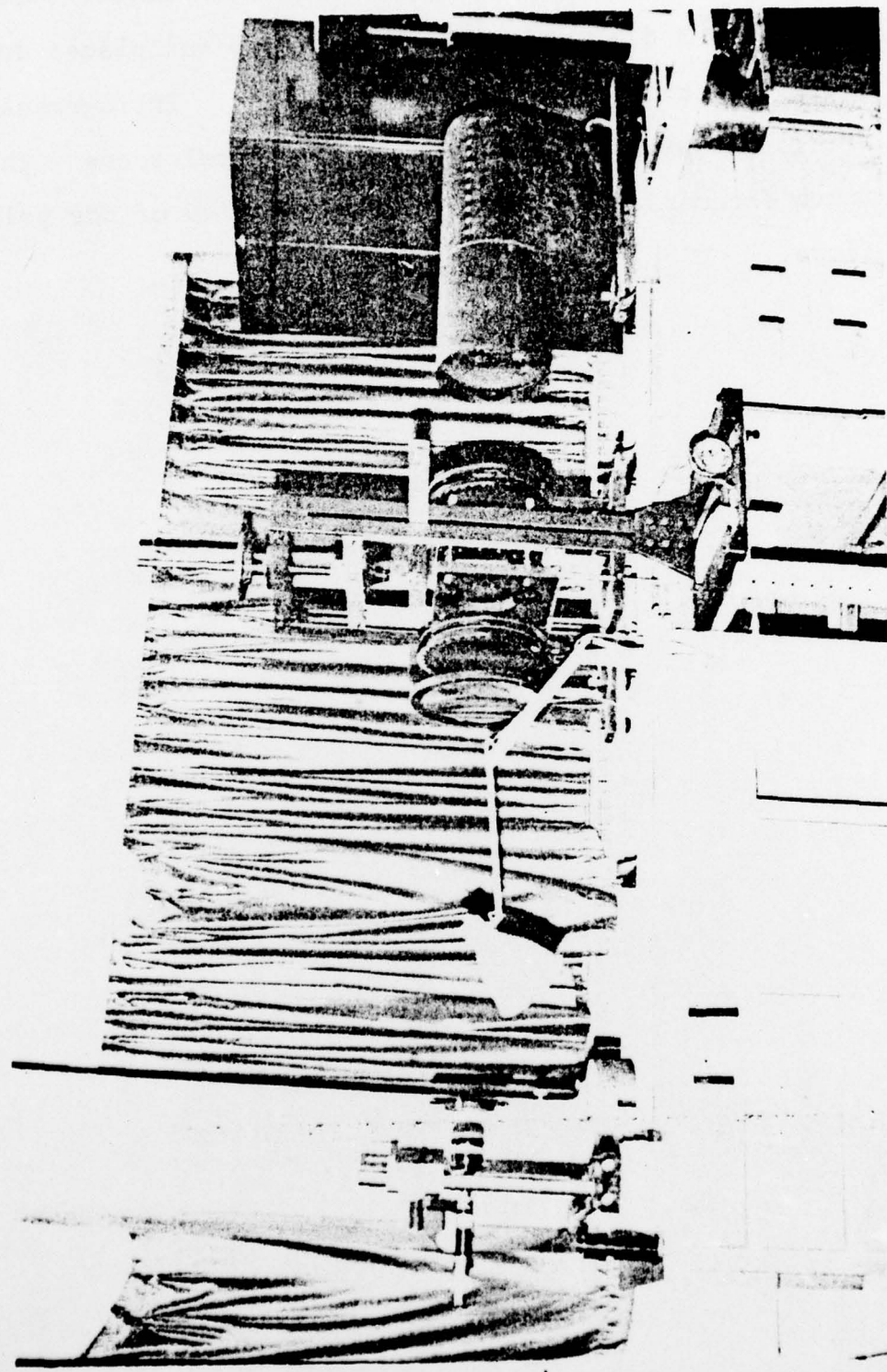


Figure A.3. Polariscope; including telemicroscope (left) and fringe multiplication unit (center).

APPENDIX B

FRINGE SHARPENING AND FRINGE MULTIPLICATION

B.1 Fringe Multiplication

Due to the low loads necessary to ensure small deformations, the resulting fringe pattern in the vicinity of the crack tip did not contain enough fringes for accurate evaluation of the stress intensity factors. A procedure known as fringe multiplication increases the fringe order at every point and produces an isochromatic pattern containing several times as many fringes as the ordinary pattern. This effect is produced by causing the light to pass through the model several times. Placing partial mirrors on both sides of the model yields multiple reflection of the light and the desired effect.

The partial mirrors are inclined to each other at a small angle. A greatly exaggerated view of the effect this has on the light path is shown in Figure B.1. The forward transmitted beams are converged by the second collimating lens to form a row of images in the focal plane at the telemicroscope. As can be seen from Figure B.1, the forward transmitted beams result in odd multiplication factors being applied to the isochromatic fringes.

It can also be seen that a certain degree of lateral travel exists between the entry and exit points of the rays.

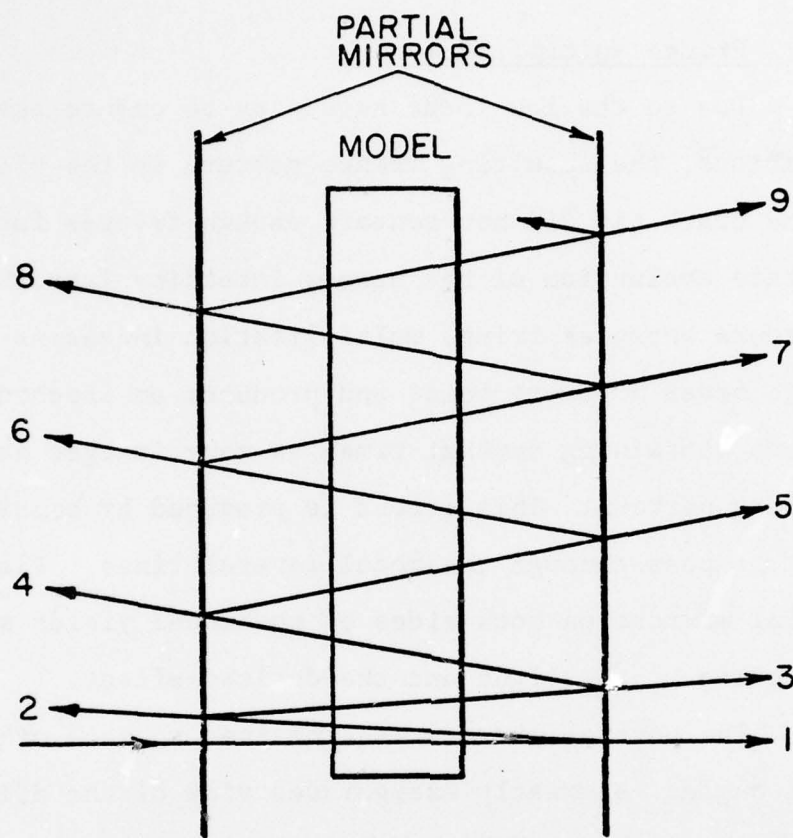


Figure B.1. Path of single light ray through
fringe multiplication unit and
model.

The observed pattern is therefore no longer representative of a single point. Reduction of the lateral travel can be achieved by rotating the entire mirror assembly so that entry and exit points on the two mirrors are opposite one another for observation of forward transmitted beams. The optimum angle of incidence required for this condition can be found by observing the images formed on the plate containing the pinhole. This row of even-numbered images is formed by the first collimating lens converging the backward transmitted rays. For observation of a certain forward directed beam, the mirror assembly is rotated until the source aperture is midway between the images of the next lower and the next higher even multiplication factors as shown in Figure B.2.

B.2 Fringe Sharpening

If the two partial mirrors are set parallel to the model, the reflected and transmitted rays are colinear with the incident ray. The intensities of the forward-directed beams are now superimposed resulting in the intensity pattern illustrated in Figure B.2. This is known as fringe sharpening because of the resulting pattern of narrow dark and bright fringes on a grey background. Fringe sharpening results in a more accurate determination of the location of isochromatics. Examples of fringe sharpening and fringe multiplication can be seen in Appendix D.

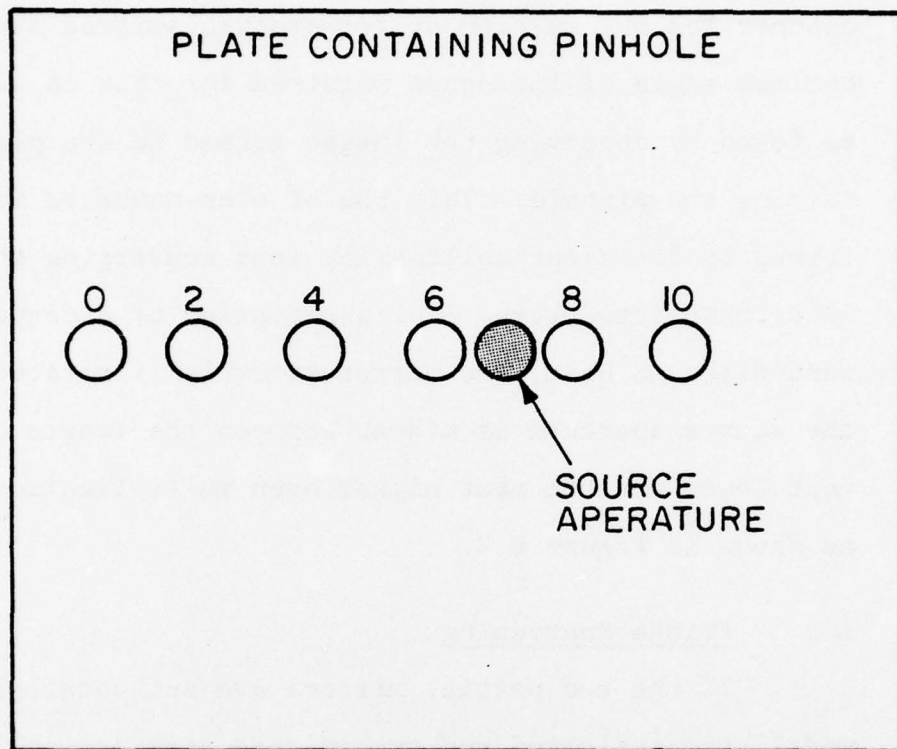


Figure B.2. Proper location of source aperture for optimum angle of incidence for a multiplication factor of seven.

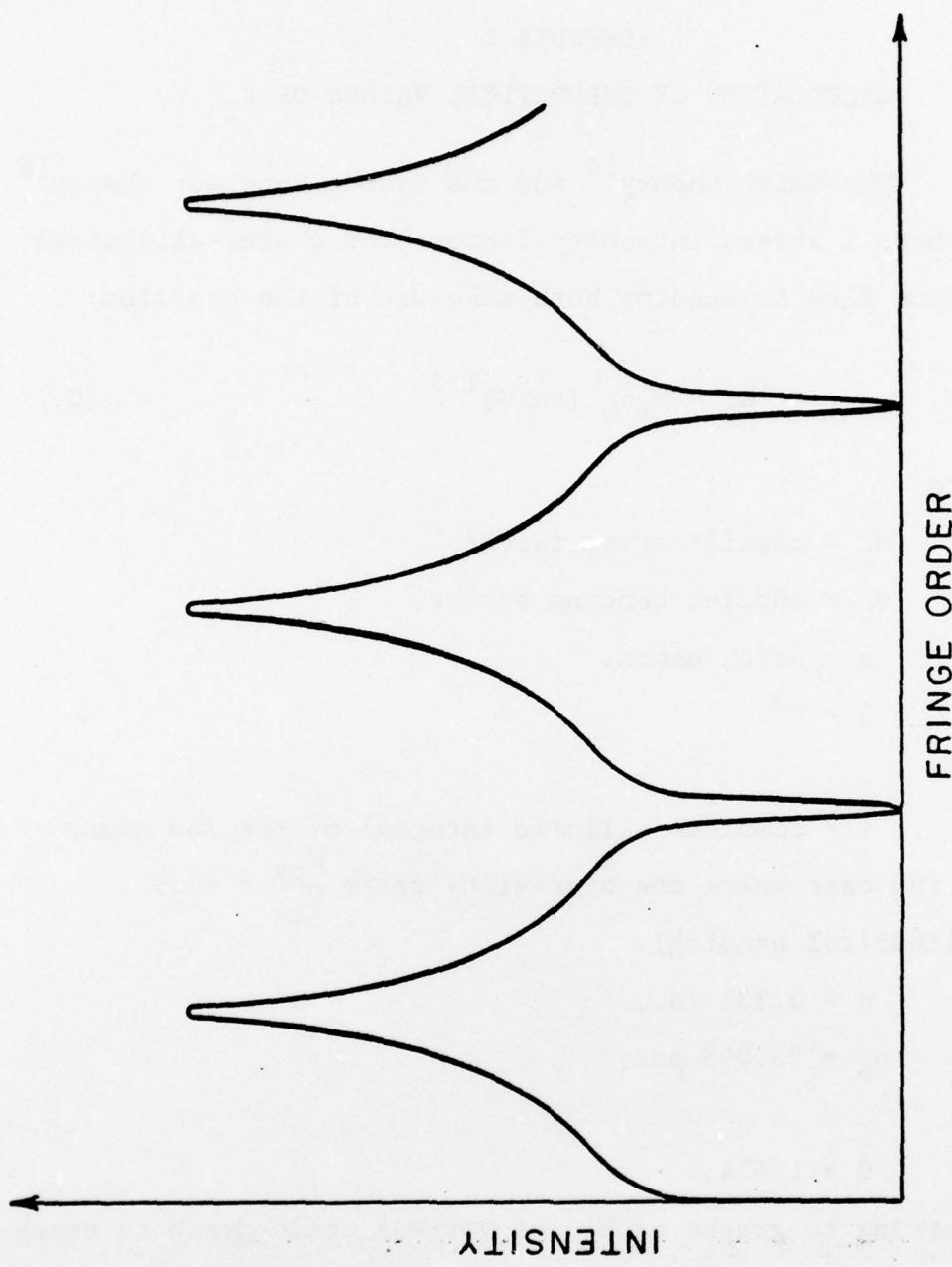


Figure B.3. Dark field intensity distribution for sharpened isochromatic fringes. After post (44).

APPENDIX C
CALCULATION OF THEORETICAL VALUES OF K_I

The Smith theory¹⁰ and the Grandt-Sinclair theory¹⁸ for Mode I stress intensity factors for a semi-elliptical surface flaw in bending both make use of the equation:

$$K_I = M_B \sigma_b [\pi a/Q]^{1/2} \quad (C.1)$$

where

M_B = magnification factor,

σ_b = applied bending stress,

a = crack depth,

$Q = \phi^2$,

and

ϕ = complete elliptic integral of the 2nd kind.

For the case where the biaxiality ratio $\frac{M_{yy}}{M_{xx}} = +0.5$
(cylindrical bending):

$a = 0.331$ in.,

$\sigma_b = 25.808$ psi,

and

$Q = 1.614$.

Referring to graphs of M_B for various crack-depth to crack-length ratios found in references 10 and 18, the following values of M_B are found:

From Grandt-Sinclair,¹⁸

$$\text{at } \alpha = 90^\circ, M_B = 0.80$$

and

$$K_I = 16.572 \text{ psi}\sqrt{\text{in.}}$$

From Smith,¹⁰

$$\text{at } \alpha = 0^\circ, M_B \approx 0.49$$

and

$$K_I = 10.15;$$

$$\text{at } \alpha = 90^\circ, M_B = 0.91$$

and

$$K_I = 18.851 \text{ psi}\sqrt{\text{in.}}$$

APPENDIX D
ISOCHROMATIC FRINGE LOOPS

Figures D.1 through D.3 illustrate photographs of several specimen slices. Included are fringe sharpening and fringe multiplication.

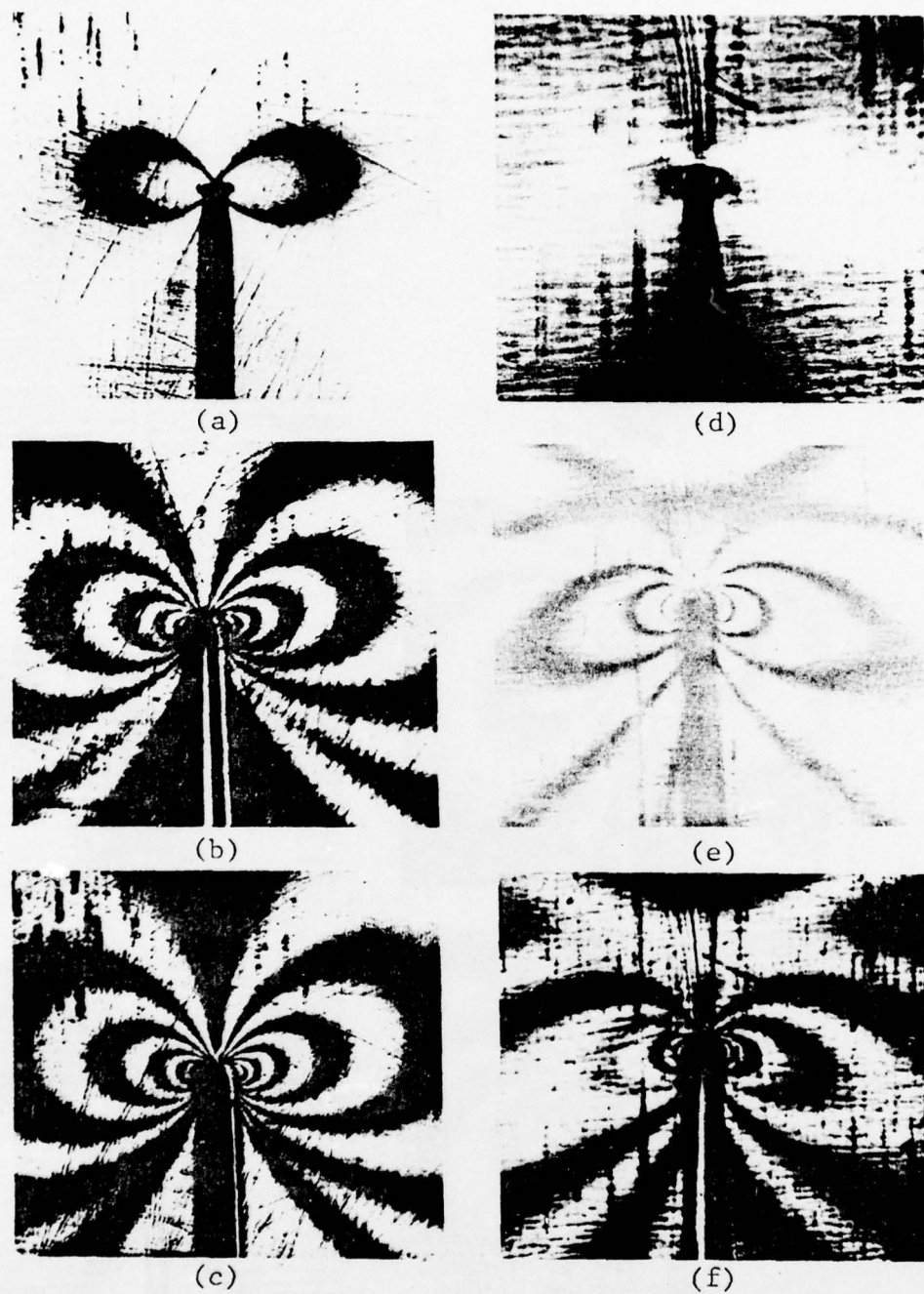


Figure D.1. Specimen No. 1; $\phi = 0.0$; $\theta = 0^\circ$

(a) $\alpha = 90^\circ$, dark field, sharpen, (b) $\alpha = 90^\circ$,
dark field, 5 X, (c) $\alpha = 90^\circ$, light field, 5 X,
(d) $\alpha = 0^\circ$, dark field, sharpen, (e) $\alpha = 0^\circ$,
dark field, 5 X, (f) $\alpha = 0^\circ$, light field, 5 X.

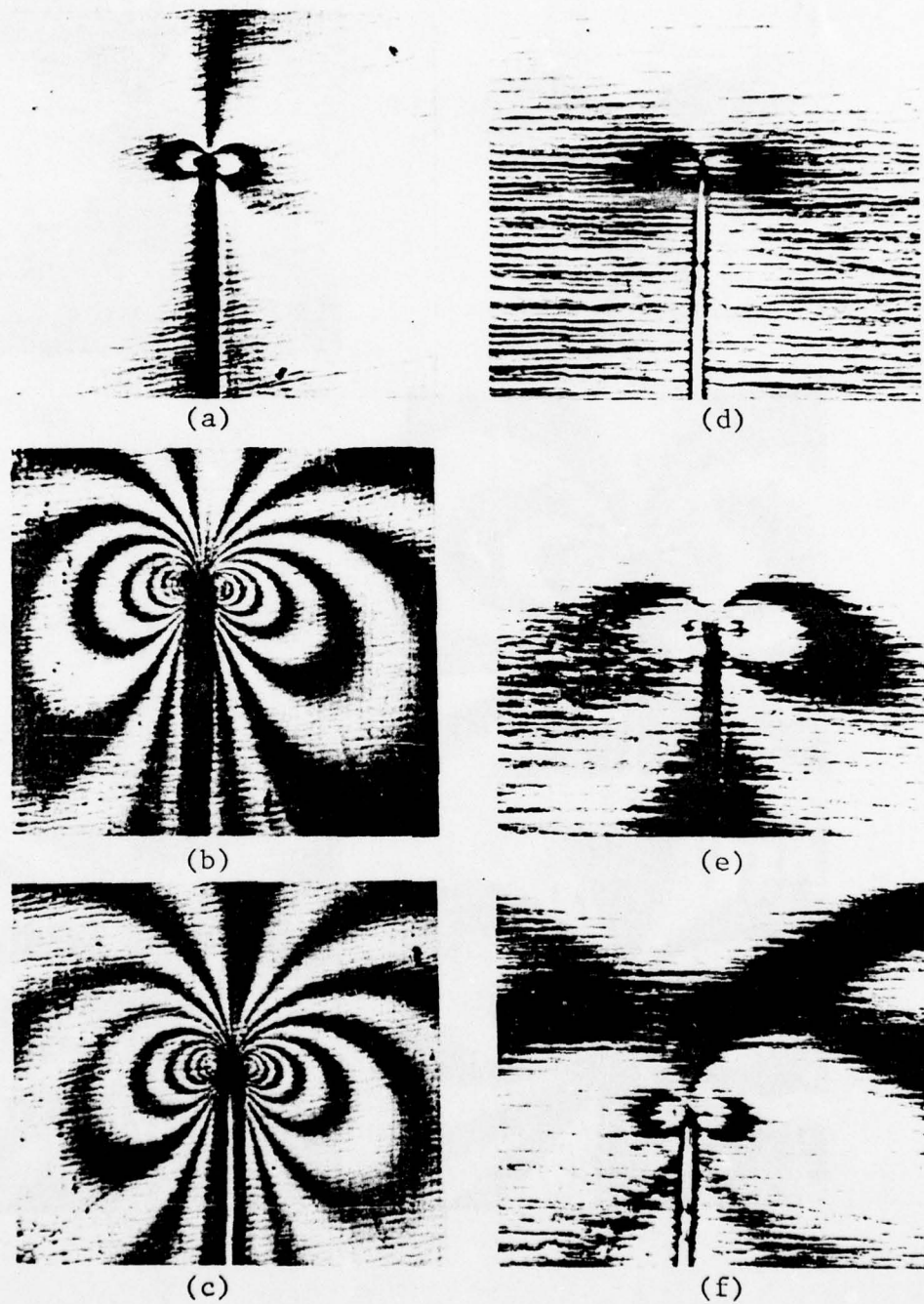


Figure D.2. Specimen No. 5; $\phi = +1.0$; $\theta = 45^\circ$

(a) $\alpha = 90^\circ$, dark field sharpen, (b) $\alpha = 90^\circ$ dark field, 7 X, (c) $\alpha = 90^\circ$, light field, 7 X, (d) $\alpha = 0^\circ$, light field, sharpen, (e) $\alpha = 0^\circ$, dark field, 3 X, (f) $\alpha = 0^\circ$, light field, 3 X.

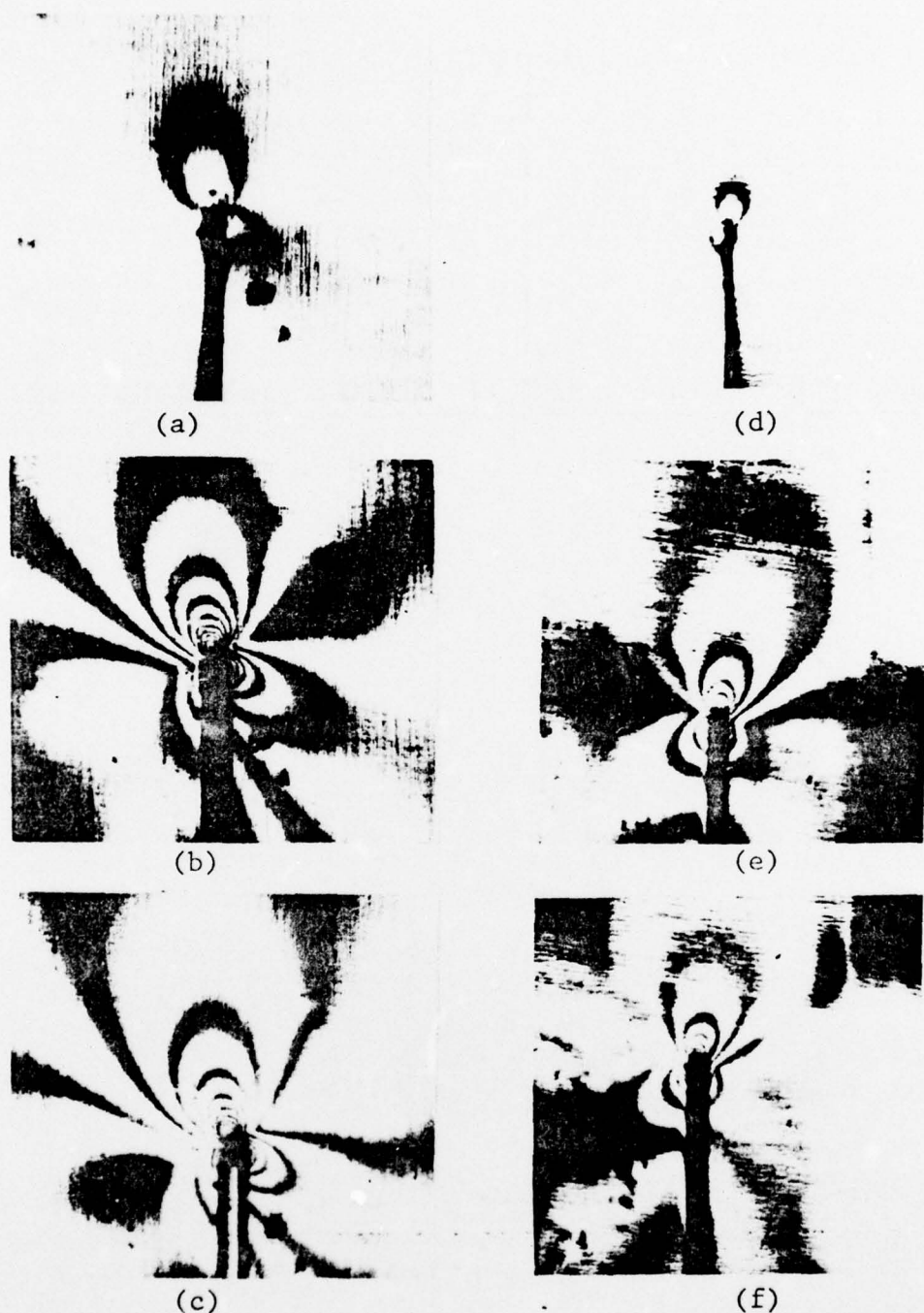


Figure D.3. (a), (b), (c) Specimen No. 4; $\phi = 0.0$; $\theta = 45^\circ$
(a) $\alpha = 90^\circ$, dark field, sharpen, (b) $\alpha = 90^\circ$, dark field,
5 X, (c) $\alpha = 90^\circ$, light field, 5 X. (d), (e), (f) Specimen
No. 8; $\phi = -1.0$, $\theta = 45^\circ$ (d) $\alpha = 90^\circ$, light field, sharpen,
(e) $\alpha = 90^\circ$, dark field, 5 X, (f) $\alpha = 90^\circ$, light field,
5 X.

DISTRIBUTION

Commander (NSEA 09G32)
Naval Sea Systems Command
Department of the Navy
Washington, DC 20362

Copies 1 and 2

Commander (NSEA 0342)
Naval Sea Systems Command
Department of the Navy
Washington, DC 20362

Copies 3 and 4

Defense Documentation Center
5010 Duke Street
Cameron Station
Alexandria, VA 22314

Copies 5 through 16